This manuscript has been submitted to *Sedimentology* for peer review. If accepted, the final version of this manuscript will be made available. Please feel free to contact any of the authors if you have any questions. Your feedback is very welcome.

Exploring the depositional, diagenetic and carbon-oxygen isotope record of an evolving Ordovician carbonate system, Tarim Basin, China

Yuefeng Shen[1*], Fritz Neuweiler[2], and Adrian Immenhauser[3, 4]

[1]*School of Resources and Environmental Engineering, Hefei University of Technology, 193 Tunxi Road, Hefei, Anhui, 230009, China, yuefengshen@hfut.edu.cn*

[2]*Department of Geology and Geological Engineering, Laval University, 1065 Avenue de la Médecine, Quebec City, Quebec, G1V 0A6, Canada*

[3]*Institute for Geology, Mineralogy and Geophysics, Ruhr-University Bochum, Universitätsstrasse 150, Bochum, D-44801, Germany*

[4]*Fraunhofer Research Institution for Energy Infrastructures and Geothermal Systems (IEG), Bochum, Germany*

[*] Corresponding author

https://orcid.org/0000-0002-6136-6802 (Y Shen)

Associate Editor – to be added by editors

ABSTRACT

Bulk-rock based carbon-oxygen chemostratigraphy should be combined with a detailed understanding of depositional facies (mineralogy, porosity), its 2D-chronostratigraphic architecture, and diagenesis. The Ordovician of the western Tarim Basin recorded a peculiar litho-biostratigraphic succession. The Darriwilian Yijianfang Formation formed part of a carbonate ramp dominated by filter feeders. Toward its top, there is condensation succeeded by a multi-Myr hiatus. The hiatus correlative succession is a black-shale (Darriwilian to early Sandbian Saergan Formation) preserved in slope-to-basin settings. A marine red-bed interval (Sandbian Tumuxiuke Formation) diachronously succeeded toward a more basin-wide record. Finally, the late Sandbian to Katian Lianglitag Formation re-established a shallow-water carbonate factory (ramp-to-platform), but this time being highly productive and hosting a diversifying assemblage of benthic primary producers. By exploring diagenesis associated with a first component-specific data-set of $\delta^{13}C$ - $\delta^{18}O$ values and by integrating and filtering respective literature bulk-rock data, a synoptic chemo-chronostratigraphic sequence is presented. It displays segments lasting from tens of Myrs to several 100 kyrs. There is a long-term trend of increasing $\delta^{13}C$ values culminating in the early Katian at 3.2 ‰ followed by a steady decrease. This tipping point is associated with a precursory baseline shift that interferes with the short-term Guttenberg carbon-isotope excursion presumably associated with a positive shift of $\delta^{18}O$ values. The baseline shift was driven by regional effects of photosynthesis and a boosting (dasycladacean-related) production of aragonite along the Sandbian-Katian boundary interval. There is a medium-term (Darriwilian to earliest Sandbian) negative $\delta^{13}C$ excursion coinciding with

both a basal positive $\delta^{18}O$ excursion and the demise of the Darriwilian carbonate ramp (*Suecicus*-Event, new term). It might represent the effects of volcanism/SO_2-outgassing during the switch from a passive to an active continental arc. This event masquerades the elsewhere recorded middle Darriwilian carbon-isotope excursion. Caution is needed to consider the Tarim realm for global Ordovician chemostratigraphy.

Keywords - Great Ordovician Biodiversification Event (GOBE), carbonate factory, drowning, black-shale, algae evolution

INTRODUCTION

Stratigraphic (incremental) organization defined by facies, geometry and architecture is an intrinsic feature of the depositional record (Ager, 1992). Following previous workers, it is suggested that carbonate depositional units are distinguished by composition, texture, the relative importance of primary skeletal mineralogy (calcite, aragonite, biogenic opal) and porosity-permeability values. In combination, these parameters result in an interval-specific diagenetic potential (reactivity), commonly studied at the ten- to several-tens-of-meter scale (Schlanger & Douglas, 1974; Flügel & Flügel-Kahler, 1992; Ausich, 1997).

During burial, a heterogeneous sedimentary succession becomes the subject of diagenetic alteration, thereby evolving into rock units. Diagenetic alteration might be stratiform, that is congruent with former depositional units (oomoldic calcarenites, stratigraphic traps; Morad *et al*., 2012) or might evolve independently *via* non-stratiform, crosscutting subsurface processes and products (mixing-zone dolomitization, thermobaric dolomitization, hydrothermal alteration, fracturing or even metamorphism; Machel, 2004; Davies & Smith, 2006; Immenhauser, 2021). The extent and variability of diagenetic alteration, whether acting within a rock- or a fluid-buffered diagenetic system (Bjørlykke & Jahren, 2012; Fantle & Higgins, 2014), in turn, determines the reliability of chemostratigraphic data (Brand & Veizer, 1981; Land, 1995 *versus* Veizer, 1995; Müller *et al*., 2020; chemostratigraphic segments of Menegatti *et al*., 1998). Depending on the proxy investigated, the parameters involved are complex, with some isotope systems potentially being rock- and others being fluid-buffered within the same rock unit (Riechelmann *et al*., 2020).

The Ordovician of the western Tarim Basin (NW China, Fig. 1) offers an outstanding case example to put the nature of the depositional, diagenetic and geochemical record of an ancient carbonate ramp to the test. Depositional units are well defined by net changes of facies (Jiao *et al*., 2012; Gao & Fan, 2013) in combination with a rapid diversification of the marine biosphere known as the Great Ordovician Biodiversification Event (GOBE, Webby *et al*., 2004). A variety of styles of diagenetic alteration is present in the Ordovician of the Tarim Basin. Most prominent examples refer to stratigraphic and structural traps related to carbonate mounds and dolostones, zones of thermobaric alteration and intense fracturing (Gao & Fan, 2013; Zhu *et al*., 2013; Zhang *et al*., 2014b; Baqués *et al*., 2020).

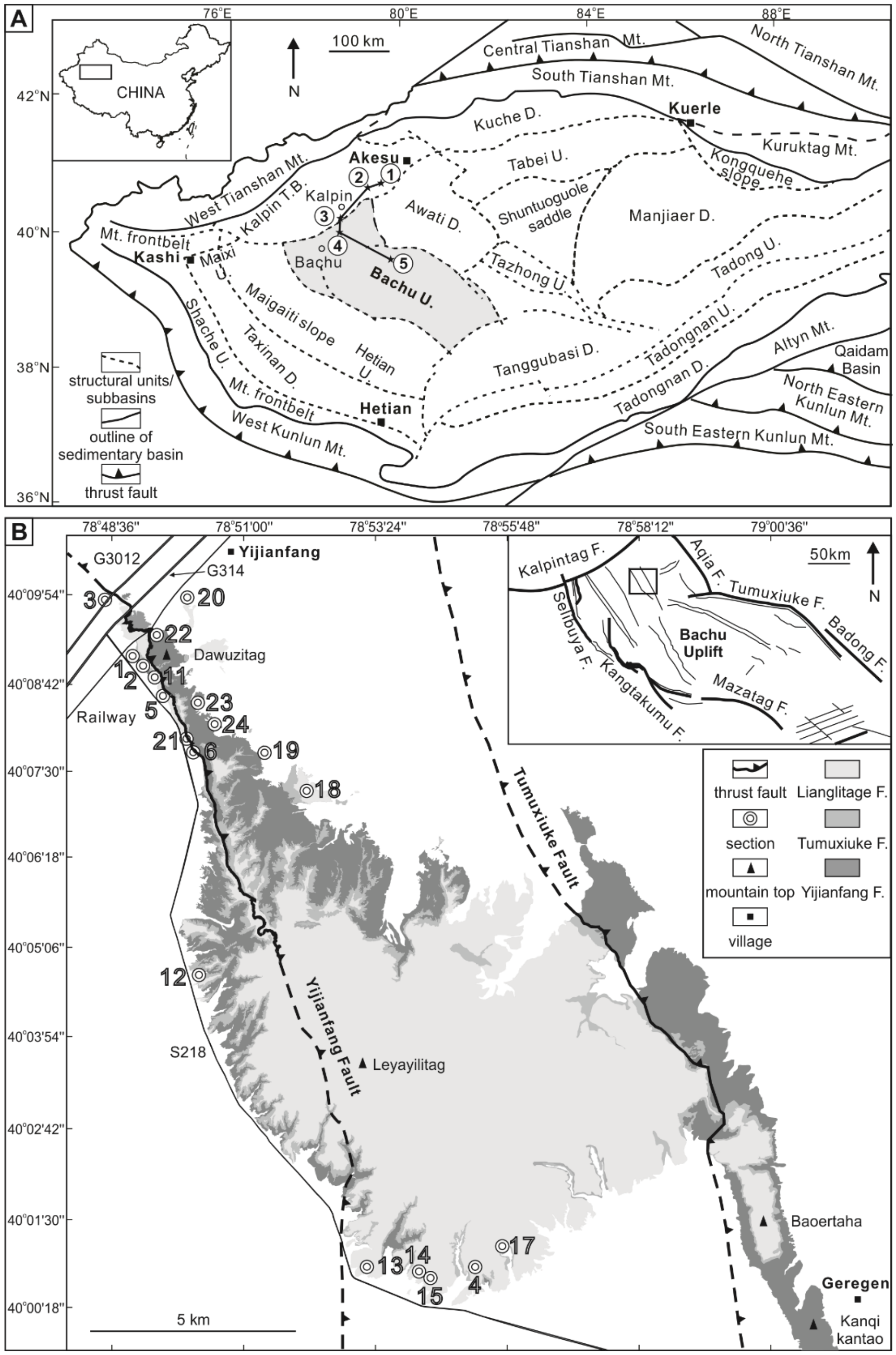

Figure—1 Study area, regional geology, and location of stratigraphic sections. **(A)** The study area is the Leyayilitag ridge (④) located east of the small village of Bachu, in the northwestern part of the Bachu Uplift, western Tarim Basin, Bachu (Maralbexi) county, Xinjiang Uyghur Autonomous Region, NW China. U.= uplift, D.= depression, Mt.= mountain belt, T.B.= thrust belt. Based on structural map of Li *et al*. (2012) and Jiao *et al*. (2012). Additional locations mentioned in the text and in figure 2 are: ①Dawangou, ②Sishichang, ③Yangjikan, ⑤Mazatag. **(B)** Geologic map of the study area and locations of stratigraphic sections (numbers for internal use). Redrawn from Li *et al*. (2012); Shen & Neuweiler (2015).

In the last decade, the Ordovician of the Tarim Basin came into the focus of chemostratigraphers searching for a global extent of $\delta^{13}C_{carbonate}$ excursions originally identified in Laurentia and Baltoscandia (Bergström *et al*., 2010a, b; Bergström *et al*., 2020). Paleogeographically, it represents the Proto-Tethyan subtropical to circum-equatorial realm; forming part of both the Paleozoic episode of evolution of the Central Asian Orogenic Belt, CAOB (Ge *et al*., 2014) and an agglomerate of terranes associated with the recently introduced Cathay-Tasman paleobiogeographic Province (Cocks & Torsvik (2020). Among the twelve Ordovician positive $\delta^{13}C_{carbonate}$ excursions (Bergström *et al*., 2020), the middle Darriwilian excursion (MDICE), the lowermost Katian Guttenberg excursion (GICE), and the Hirnantian one (HICE, not dealt herein) are most prominent (Algeo *et al*., 2016; Bergström *et al*., 2020). These positive $\delta^{13}C_{carbonate}$ excursions can be considered a stepwise prelude (CO_2 drawdown, cooling) to the End-Ordovician (Hirnantian) icehouse (summary and critique in Quinton, 2016).

There were several attempts to identify and track the MDICE and the GICE in the Tarim Basin. Bergström *et al*. (2009) re-used original data of Jiang *et al*. (2001) whereas Rong *et al*. (2014) re-used original data of Zhao *et al*. (2009, 2010). Zhang & Munnecke (2016), as well as Liu *et al*. (2016a) presented evidence stretching over almost the full stratigraphic range of the Ordovician and concluded that the Proto-Tethyan $\delta^{13}C_{carbonate}$-chemostratigraphy is in accord with that proposed for the Iapetus Ocean (essentially Baltica and Laurentia). However, a number of the above author's chemostratigraphic labels appear problematic in terms of shape, magnitude and/or age why they frequently hold a question mark (Zhang & Munnecke, 2016). Beyond problematic graphic correlation, the underlying steering mechanisms of Ordovician $\delta^{13}C_{carbonate}$ excursions are still poorly understood (Bergström *et al*., 2010a; Zhang & Munnecke, 2016; Bergström *et al*., 2020).

Strikingly, in the Tarim Basin, *hitherto* the chemostratigraphic data set of $\delta^{13}C_{carbonate}$ (DIC) and $\delta^{18}O_{carbonate}$ values relies exclusively on bulk-rock geochemical samples. With the exception of Baqués *et al*. (2020) work, there is no systematic study applying component-specific (skeletons, non-skeletal particles, cements, replacive phases) geochemical analysis in combination with a detailed analysis of the diagenetic history. Indeed, apparently good evidence for a positive $\delta^{13}C_{carbonate}$ excursion (whether MDICE or GICE) exists only locally, elsewhere it appears facies-dependent (Zhang & Munnecke, 2016), severely indistinct (Liu *et al*., 2016a) or is absent (Jiang *et al*., 2001). Yet, no study established a concurrent cooling trend, for example, an associated rise of $\delta^{18}O_{carbonate}$ or $\delta^{18}O_{conodont\ apatite}$ that should exist if the MDICE or the GICE were properly identified and understood (Quinton *et al*., 2018).

This paper deals with a hierarchical (step-by-step) set of objectives. First, the nature of depositional, diagenetic and geochemical ($\delta^{13}C$; $\delta^{18}O$) units is explored in terms of complexity and degree of correspondence. Second, the informative value of the *hitherto* published bulk-rock geochemical data set is critically re-assessed (filtered) by comparing it with the herein presented first component-specific set of the preserved carbon- and oxygen-isotope ratios (virtual mixing, depositional *versus* diagenetic values, noise *versus* anomaly). Third, an adjusted synoptic chronostratigraphic plot (Wheeler diagram) of Middle to Late Ordovician carbon- and oxygen-isotope values (own data plus filtered literature data) then should serve to discriminate long-term trends, medium-term patterns and short-term geochemical events (purported MDICE, GICE; datum, shape, magnitude). Finally, a discussion on the potential steering mechanisms is presented, from regional to a global scale, in terms of a rapidly evolving biosphere, carbon cycling, and the various modes and scales of carbonate sediment production.

STUDY AREA AND STRATIGRAPHIC ARCHITECTURE

The study area is the Dawuzitag-Leyayilitag ridge near the northwestern limit of the Bachu Uplift, western Tarim Basin, Bachu (Maralbexi) county, Xinjiang Uyghur Autonomous Region, NW China (Fig. 1). The Dawuzitag-Leyayilitag ridge is bounded by the NW-SE striking Yijianfang-Tumuxiuke fault system and the NNE-SSW striking Kalpintag thrust-fault belt (Turner *et al*., 2010; Fig. 1). From base to top, the locality exposes four Ordovician carbonate formations (Fig. 2): the upper part of the Yingshan, the Yijianfang, the Tumuxiuke and the lower part of the Lianglitag formations (Shen & Neuweiler, 2015, 2016; Zhang & Munnecke, 2016). The succession has a total stratigraphic thickness of about 150 meters.

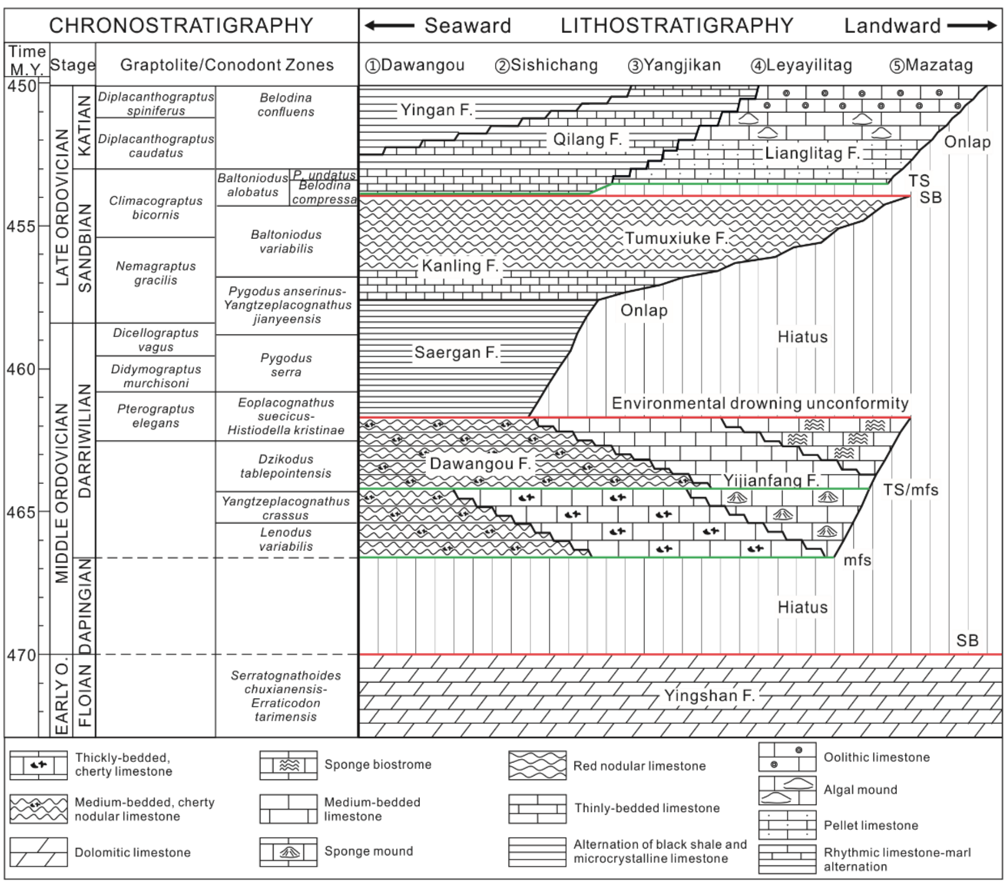

Figure—2 Time-stratigraphic cross section (Wheeler diagram) of the Ordovician of the western Tarim Basin; see Fig. 1 for location of key sections. Compiled from Li *et al*. (2009); Ma *et al*. (2013); Zhang *et al*. (2015); Zhang & Munnecke (2016); Wang *et al*. (2017b); Li *et al*. (2017); Shen & Neuweiler (2018). SB = sequence boundary, TS = transgressive surface, mfs = maximum flooding surface.

The upper part of the Yingshan Formation (Floain according to Wang *et al*., 2017b; Zhao *et al*., 2018) is an alternation of micritic limestone and dolostone. There is an unconformity between the Yingshan Formation and the Yijianfang Formation defined by erosion, karstification, and brecciation (Li *et al*., 2007, 2009; Zhang *et al*., 2014a, 2015; Zhang & Munnecke, 2016; Wang *et al*., 2017b; Zhao *et al*., 2018; Figs. 2-4). The Yijianfang Formation is a succession from calathid-demosponge carbonate mounds and bioclastic limestone to biostromal deposits (Figs. 2-4). This unit contains, in ascending order, the *Lenodus variabilis*, the *Yangtzeplacognathus crassus*, the *Dzikodus tablepointensis*, the *Eoplacognathus suecicus* and the *Pygodus serra* conodont Zone, altogether indicating a Darriwilian age (*ca* 467-458 Ma; Zhou *et al*., 1990; Wang & Zhou, 1998; Zhao *et al*., 2000; Xiong *et al*., 2006; Li *et al*., 2009; Wang *et al*., 2017b; Zhao *et al*., 2018). The Tumuxiuke Formation (Qiaerbak or Kanling Formation of others) overlies disconformably the Yijianfang Formation (major hiatus; drowning unconformity according to Wang *et al*., 2017b) and consists of reddish nodular limestone (Figs. 2-4). This unit contains three conodont biozones, namely the *Pygodus anserinus-Yangtzeplacognathus jianyeensis*, the *Baltoniodus variabilis* and the *Baltoniodus alobatus* Zone indicating a Sandbian age (*ca* 458-453 Ma; Xiong *et al*., 2006; Wang *et al*., 2017b; Zhao *et al*., 2018). The Lianglitag Formation succeeds after a minor hiatus (Wang *et al*., 2017b; Figs. 2-4). It is a succession of grey to reddish, nodular, bedded to massive limestone (Figs. 2-4). The conodonts of the Lianglitag Formation essentially belong to the *Belodina confluens* Zone indicating an early to middle Katian age (*ca* 453-450 Ma; Wang & Zhou, 1998; Li *et al*., 2009; Wang *et al*., 2017b; Zhao *et al*., 2018).

The local depositional sequence (Figs. 2-4) forms part of a carbonate ramp that deepens over about 50 km from the Leyayilitag region into the northern basinal settings of the Dawangou region (Figs. 1, 2; Li *et al*., 2009; Zhang *et al*., 2015; Wang *et al*., 2017a; Li *et al*., 2017; Shen & Neuweiler, 2018). The Yangjikan region marks the transitional zone toward outer-ramp-to-basinal settings (Figs. 1, 2; Ma *et al*., 2013). The Darriwilian is absent in the Mazatag region (Figs. 1, 2; well-log data reported by Wang *et al*., 2017b). The Katian Lianglitag Formation evolved rapidly from an initial ramp into a highly productive shoal-rimmed carbonate platform.

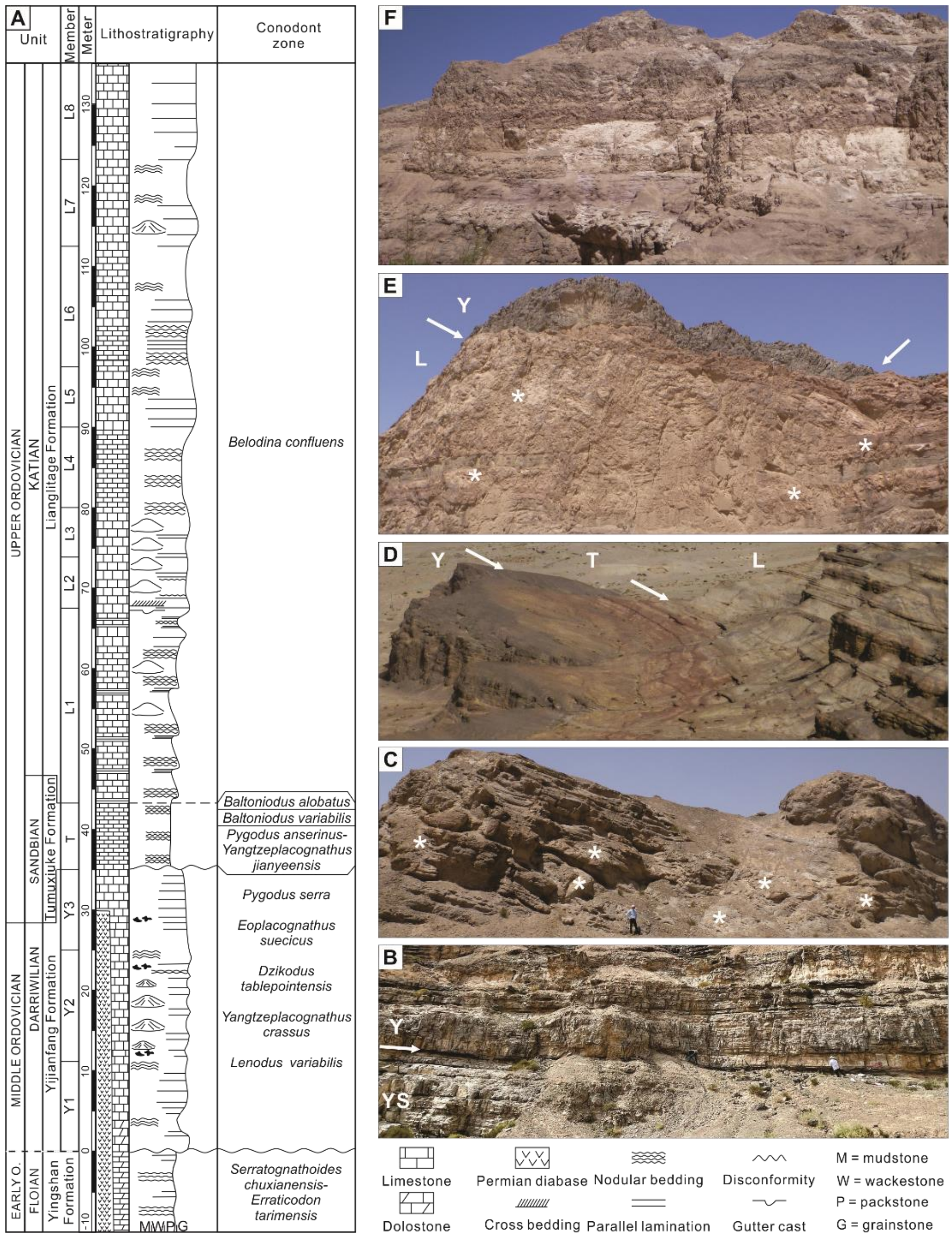

Figure—3 Stratigraphy and field views of the Ordovician of the Leyayilitag ridge. **(A)** Bio- and lithostratigraphy compiled from Zhou *et al*. (1990); Wang & Zhou (1998); Zhao *et al*. (2000); Xiong *et al*. (2006); Li *et al*. (2009); Jiao *et al*. (2011); Wang *et al*. (2017b); Zhou *et al*. (2018) and own observations. **(B-F)** Field views of major lithostratigraphic units: **(B)** Upper part of the Yingshan Formation (YS) composed of fine-grained limestone and lower part of the Yijianfang Formation (Y) composed of bedded bioclastic limestone (arrow = boundary). **(C)** Middle part of the Yijianfang Formation exposing calathid-demosponge carbonate mounds (*) and bedded encrinitic limestone (second author for scale). **(D)** Upper part of the Yijianfang Formation (Y) composed of sponge biostromes and bioclastic limestone succeeded by the reddish, nodular limestone of the Tumuxiuke Formation (T) and a rhythmic succession of (argillaceous) limestone characterizing the lower part of Lianglitag Formation (L). **(E)** The first member of the Lianglitag Formation (L) hosting patchy carbonate mounds (*) and reefal (algal) limestones (*). Arrows point on the Yijianfang thrust fault; Y = Yijianfang Formation. **(F)** The second member of the Lianglitag Formation consists of varicolored (white, grey, reddish, mauve) massive, bedded and nodular limestone.

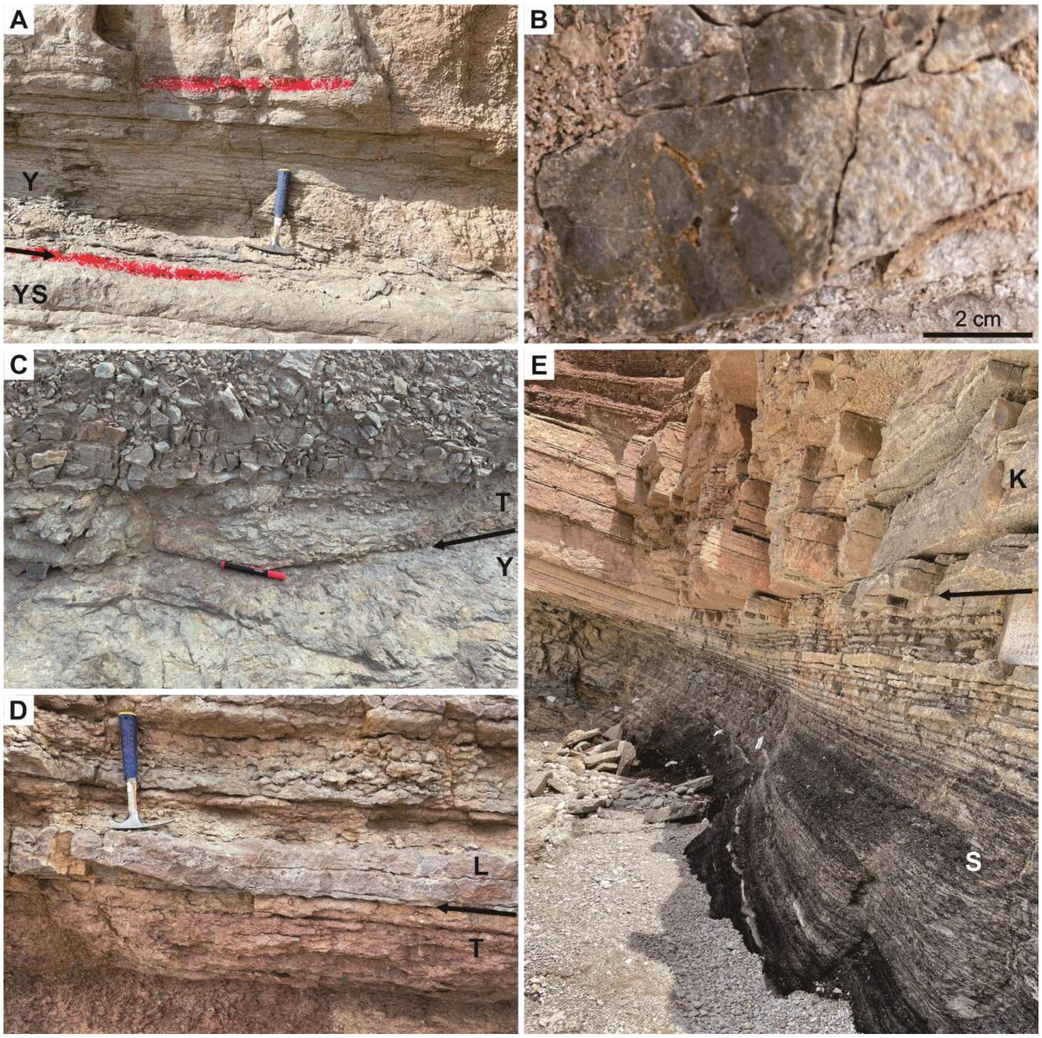

Figure—4 Key lithostratigraphic units of Bachu-Kalpin area. **(A)** The uppermost part of the Yingshan Formation (YS) represents a subaerial exposure surface (brecciated paleokarst). The lowermost part of the Yijianfang Formation (Y) is composed of laminated limestone. Arrow = boundary; hammer for scale. **(B)** Brecciated top of the Yingshan Formation. **(C)** The boundary (arrow) between the Yijianfang (Y) and Tumuxiuke (T) formations represents a drowning unconformity. **(D)** Boundary (arrow) between the Tumuxiuke (T) and Lianglitag (L) formations. **(E)** Boundary (arrow) between the Saergan Formation (S) composed of black-shale and an alternation of black shale and microcrystalline carbonate and the Kanling Formation (K) composed of reddish nodular limestone.

MATERIAL AND METHODS

Fieldwork and Sampling

One hundred sixty-eight rock samples were collected from nineteen stratigraphic sections (Fig. 1; details in supplementary data files of Shen & Neuweiler, 2016). One-hundred thirty thin sections were prepared. Forty-one of these were stained with alizarin red-S. Another twenty-six thin sections were stained using a combination of alizarin red-S and potassium ferricyanide (Dickson, 1965). Thirty-four thin sections were examined by both fluorescence and cathodoluminescence microscopy. From their corresponding opposite side (polished slabs), sub-samples for geochemical analysis were drilled. Geochemical sampling was performed using a computer-controlled microdrill (CAM system) with a drill-head diameter of 1 mm. In some cases, microsampling was performed using a micromill system with a resolution of 100 μm (Mechantek, esi/New Wave, Dettman & Lohmann, 1995).

Petrographic and Geochemical Analyses

Petrography was performed using a Leica Z6 APO macroscope and a Leitz Orthoplan microscope, both equipped for normal and polarized transmitted light and a Zeiss Axiocam camera. An assessment of the primary depositional mineralogy (relative importance of high-Mg calcite, low-Mg calcite, aragonite, biogenic opal) was achieved using a combination of petrographic attributes such as form, design, microstructure, microdolomite inclusions, pseudospar and calcite-cemented molds. Fluorescence microscopy (ZEISS) was performed at excitation of 450–490 nm and emission > 520 nm. Cathodoluminescence microscopy was performed with both a cold Nuclide Corporation model EEM2E luminoscope (12–18 kV, 0.5 mA, beam focused at 5 mm) and a hot-cathode luminescence microscope (14 kV, current density at 10 μA/mm^2) on gold-coated thin sections (Neuser *et al*., 1995; Richter *et al*., 2003). For scanning electron microscopy (SEM), twenty-four samples were polished using a 6-µm-diamond paste. These samples were then treated with boiling 0.2 M EDTA for one to two hours (Bodine & Fernalld, 1973). The SEM is a JEOL 840-A equipped with a NORAN light-elements energy-dispersive analytical system. Carbon ($\delta^{13}C$) and oxygen ($\delta^{18}O$) isotopic composition was determined using a continuous flow Thermo Finnigan GasBench coupled to a DeltaPlus XP IRMS. The $\delta^{18}O$ and $\delta^{13}C$ isotope data are presented in ‰ relative to the Vienna Pee Dee Belemnite standard (V-PDB) with an analytical precision (σ) of 0.1 ‰ points.

Generation of Virtual Bulk Samples

For each lithosome, the component-specific isotope data were organized into categories of depositional/early diagenetic, shallow burial and deep (late) burial origin and respective means and standard deviations were determined. In a second step, for each of those categories the range of rock vol-% was assessed (min/max; data weighting). For the Yijianfang Formation, the depositional/early diagenetic and shallow burial categories were assessed to range between 45-60% and 25-35%, respectively. For the Lianglitag Formation, the depositional/early diagenetic and shallow burial categories were assessed to range between 40-60% and 20-35%, respectively. Due to its essentially microcrystalline nature, for the Tumuxiuke Formation only Gaussian scattering was performed. The Random Number Generation tool of MS Excel was used (normal distribution for range of isotope data; linear distribution for rock vol-%) and the resulting means and standard deviations (3σ) of the random mixtures were determined.

RESULTS

The Depositional Record

A combination of facies analysis (twenty-five facies units, Table 1), depositional geometries and stacking patterns, primary mineralogy (aragonite, low Mg-calcite, high Mg-calcite, biogenic opal) and primary to early secondary porosity resulted in the definition of four depositional units (Table 1). The Yijianfang Formation is a combination of sponge carbonate mound, encrinite and sponge biostrome (~35 m thick); the Tumuxiuke Formation is a marine red bed interval (e.g., Song *et al*., 2017) about 10 m thick; the first member of the Lianglitag Formation (L1) is a combination of a variety of algal mounds embedded in pelletal limestone (~35 m thick); the second member of the Lianglitag Formation (L2) corresponds to ooid-rich peritidalites (~50 m thick).

Table—1 Facies units (FU) by formation and member present in the Middle to Late Ordovician succession at Bachu Uplift, western Tarim Basin, Bachu (Maralbexi) county, Xinjiang Uyghur Autonomous Region, NW China.

Formation	FU	Classification	Diagnostic criteria
Yijianfang Formation	FU1	Bioclastic pack- to grainstone	Fine-grained, medium-sorted. Composed of crinoid ossicles, molluscan shells and spicules of siliceous sponges. Accessory: trilobite hash, ostracods,*Girvanella*.
	FU2	Bioclastic packstone	Fine- to medium grained, medium-sorted. Composed of abundant crinoid ossicles and crinoid fragments with *Girvanella*. Accessory: bryozoa, trilobites, ostracods, brachiopods.
	FU3	Calathid-demosponge-automicrite boundstone	Calathids with abundant demosponges preserved as automicrite (Shen and Neuweiler, 2018). Accessory: crinoid ossicles, bryozoa, *Girvanella*, *Wetheredella*, *Halysis*, *Moniliporella*, brachiopods, molluscs, trilobites and *Pulchrilamina*.
	FU4	Bioclastic wacke- to packstone	Poorly-sorted infiltrated sediment within FU3. Contains parautochthonous debris of crinoids and bryozoa. Accessory: trilobites, ostracods, bivalves, *Girvanella*, *Moniliporella*.
	FU5	Bioclastic float- to rudstone	Poorly-sorted mound debris composed of (fragmented) calathid sponges and automicritic demosponges. Abundant crinoid fragments and ossicles.
	FU6	Encrinitic pack- to grainstone	Poorly-sorted and coarse-grained. Abundant parautochthonous crinoid fragments. Accessory: bryozoa, trilobite hash.
	FU7	Crinoidal pack- to grainstone	Well-sorted and fine-grained. Abundant crinoid ossicles, minor crinoid fragments. Accessory: bryozoa, *Girvanella*, *Nuia*, *Halysis*, brachiopods and trilobite hash.
	FU8	Bioclastic grainstone	Well-sorted and fine-grained. Composed of crinoid ossicles, peloids, trilobite hash, bivalves, spicules of siliceous sponges, *Girvanella*.
	FU9	Calathid sponge biostrome	Calathid sponges in association with some automicritic demosponges, crinoid fragments, bryozoa, sponge spicules, bivalves. Peloid-rich sedimentary matrix.
	FU10	Encrinitic wacke- to packstone (glauconitic)	Bimodal association of uniformly small-size ossicles in micrite. Accessory: sponge spicules, ostracods, gastropods, granular phosphate and green mica. Mottled fabric, open burrows.
Tumuxiuke Formation	FU11	Nodular bioclastic wackestone	Marine red bed. Composed of large ostracods, thin-shelled molluscan debris, some crinoid ossicles and (heavily stained) intraclasts. Accessory: nautilids, trilobite hash, brachiopods.

	FU12	Bioclastic-peloidal wacke- to packstone	Marine red bed, reddish to grey, nodular. Composed of ostracods, bryozoa and (micro-) bioclasts of trilobites, crinoids and thin-shelled molluscs (incl. nautilids).
Lianglitag Formation (L1)	FU13	Algal-calcimicrobial boundstone	Association of *Vermiporella*, *Girvanella*, *Halysis*, *Apidium*, *Moniliporella*, *Arthroporella*, *Subtifloria*, *Rothpletzella*, *Rauserina* and *Renalcis*.
	FU14	*Vermiporella* boundstone	Accessory: some calcimicrobes and other calcareous algae. Matrix is a pellet-rich pack- to grainstone. Bioclasts of crinoids, gastropods, ostracods and trilobites.
	FU15	*Arthroporella* boundstone	Accessory: some calcimicrobes and other calcareous algae. Matrix is a pellet-rich pack- to grainstone. Bioclasts of crinoids, gastropods, ostracods and trilobites.
	FU16	Pellet grainstone with abundant *Halysis*	Large fragments of *Halysis* embedded in a grainstone matrix with bioclasts of crinoids, gastropods, ostracods and trilobites. Shelter- and sagging pores (Shen and Neuweiler, 2015).
	FU17	Well-sorted algal-pellet pack- to grainstone	Fragments of *Apidium*, *Moniliporella*, *Vermiporella*, *Dasyporella*, *Aphroporella*, *Girvanella*, *Subtifloria*, *Renalcis*, *Phacelophyton* and *Wetheredella*. Some ooids, ossicles, ostracods.
	FU18	*Palaeoporella* boundstone	*Palaeoporella* associated with *Mastopora*, *Apidium*, *Halysis*, *Girvanella* and *Rothpletzella*. Algal-pellet grainstone matrix with bioclasts of brachiopods, bryozoa, ostracods, trilobites.
	FU19	Calcimicrobial-sponge boundstone	Association of *Renalcis*, siliceous sponges and encrusting bryozoa. Some ostracods and trilobite hash.
Lianglitag Formation (L2)	FU20	Algal-pellet grainstone	Accessory: oncoids, ooids, grapestones. Small bioclasts of trilobites, bryozoa, ostracods, gastropods, *Phacelophyton, Girvanella*, *Garwoodia*, *Ortonella*, *Vermiporella*, *Arthroporella*.
	FU21	Oncoid grainstone	Nuclei of oncoids are compound ooids, pellets or fragments of calcimicrobes (*Hedstromia*, *Bija*). Some pellets and ooids.
	FU22	Ooid grainstone	Nuclei of ooids are pellets or fragments of *Garwoodia*, *Bija*, *Hedstromia*, *Ortonella*. Some pellets and aggregate grains.
	FU23	Oolitic calcimicrobial bindstone	*Ortonell*a and *Garwoodia* in association with ooids and pellets. Some dissolution enhanced bird's eyes.
	FU24	Cryptalgal peloid pack- to grainstone	Cryptalgal pack- to grainstone with fenestrae, bird's eyes and keystone vugs. Some bioclasts of bivalves, trilobites, ostracods.
	FU25	Intraclastic grainstone	Intraclasts of cryptalgal pack- to grainstone (FU24). Some molluscan debris.

Yijianfang Formation

The Yijianfang Formation comprises ten facies units (Table 1; Figs. 3, 5). In terms of the primary mineralogy, there is a volumetric importance of low-Mg calcite ≈ high-Mg calcite > biogenic opal > aragonite. Based on thin-section evaluation, the low-Mg calcite facies comprises automicrite and a number of skeletons such as bryozoans, brachiopods, trilobites, as well as calcimicrobes. High-Mg calcite derives from pelmatozoan debris, biogenic opal from siliceous sponges (demosponges); aragonite from calathid sponges and a variety of molluscs (bivalves, nautilids, gastropods). Porosity at deposition corresponds to residual growth cavities present in sponge carbonate mounds, to interparticle porosity of encrinitic grainstones and a combination of both in sponge biostromes (Fig. 5). Early secondary (moldic) porosity developed in calathid sponges and, to a minor degree, in molluscs and siliceous sponge spicules (Fig. 5).

Approaching the drowning unconformity that marks the top of the Yijianfang Formation, a peculiar facies accumulated. There is a poorly-sorted, fine-grained bioclastic wacke- to packstone composed of strikingly small, parautochthonous crinoid debris and ossicles (Fig. 5E-F). Shelly material and sponge spicules are accessory. The deposit contains aggregates of green clay minerals (presumably glauconite, chamosite), phosphorite, a mottled (bioturbated) fabric and some open burrows with agglutinated fringe (Fig. 5E-F). This facies anomaly goes along with the extinction of calathid sponges thereby recording the successive demise of the Yijianfang calathid-demosponge-crinoid carbonate factory.

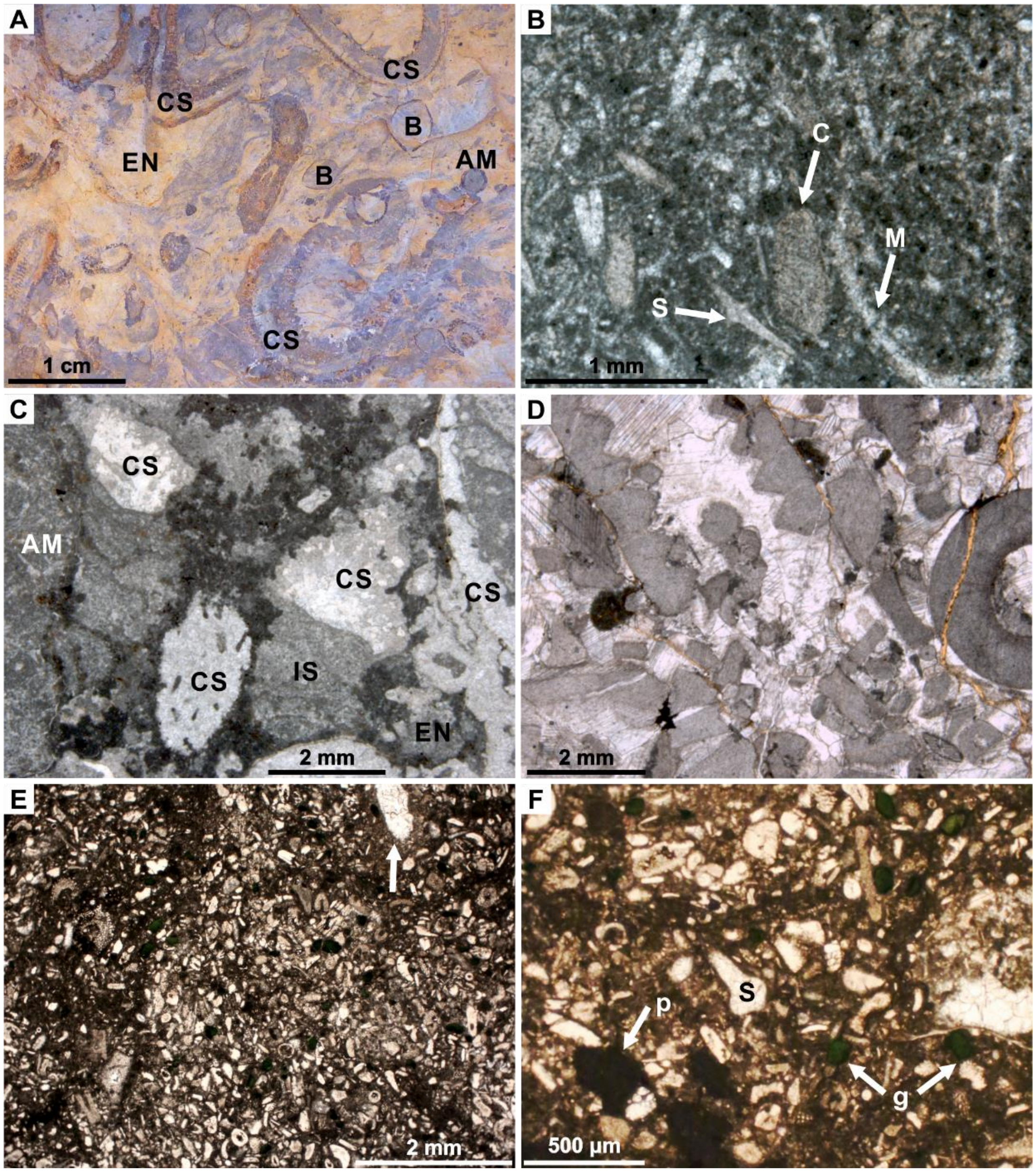

Figure—5 The Yijianfang Formation, key facies units (FU); **(A)** outcrop, **(B-F)** thin-section micrograph. **(A)** FU3 is a calathid-demosponge-automicrite boundstone; calathid sponges (CS), automicrite associated with siliceous sponges (AM), brachiopods (B) and a fine-grained encrinitic matrix (EN). **(B)** FU1 is a fine-grained, medium-sorted bioclastic pack- to grainstone, C = crinoid ossicle; M = cemented mold of gastropod shell; S = cemented mold of siliceous sponge spicule. **(C)** Calathid-demosponge-automicrite boundstone (FU3) in thin section, cf. **(A)**. Calathid sponges (CS); automicritic demosponge (AM); encrinitic matrix (EN). There is sediment infiltration (IS) penecontemporaneous with aragonite dissolution and marine cement precipitation. **(D)** FU6 is a coarse-grained, poorly sorted encrinite (pack- to grainstone) with parautochthonous skeletal debris. **(E)** FU10 is a bimodal encrinitic wacke- to packstone with granular phosphate and granular green mica (purported glauconite). There is a mottled fabric and some open burrows with agglutinated walls (arrow). Note the narrow size range of the crinoid ossicles. This peculiar facies evolves in the uppermost part of the Yijianfang Formation approaching the drowning unconformity. **(F)** Close-up of **(E)** displaying granular phosphate (p) and granular green mica (g); S = sponge spicule.

Tumuxiuke Formation

The Tumuxiuke Formation is composed of thinly-bedded to nodular, brownish to reddish argillaceous limestone and comprises two facies units (Table 1; Figs. 3, 6). There is a volumetric importance of low-Mg calcite >> aragonite ≥ high-Mg calcite. Low-Mg calcite derives from micrite, peloids and a variety of skeletal debris (trilobites, ostracods, bryozoans, brachiopods). Aragonite refers to molluscs such as gastropods, nautilids and bivalves; high Mg-calcite stems from crinoid ossicles. Some lithoclasts bear iron-rich oncoidal envelopes (Figs. 6B, 14A). Primary porosities relate to both some shelter and intraparticle pores in bioclastic packstone and generalized matrix porosity. Moldic porosity refers to aragonitic molluscan biominerals.

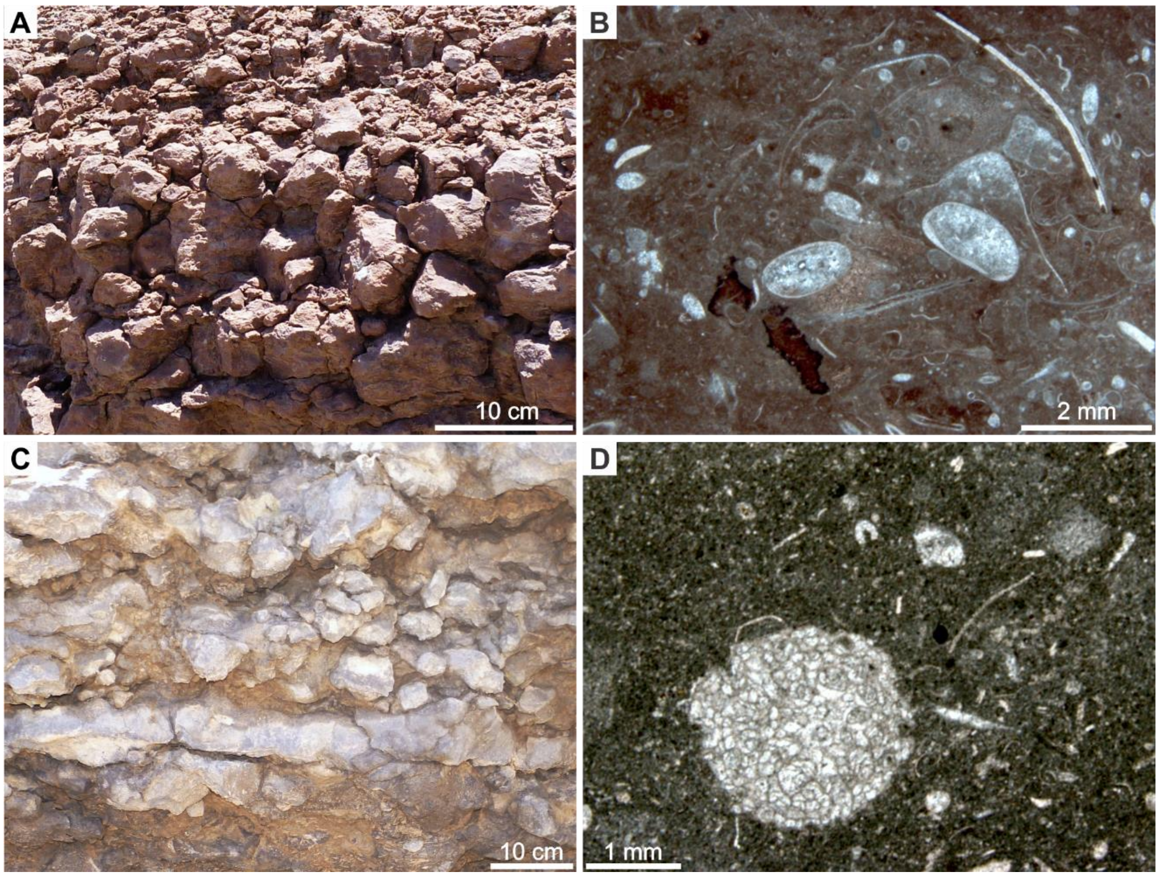

Figure—6 The Tumuxiuke Formation (condensed section), key facies units (FU), **(A, C)** outcrop; **(B, D)** thin-section micrograph. **(A)** Heavily weathered, reddish nodular limestone. **(B)** The respective microfacies (FU11) is a bioclastic wackestone with large ostracods, thin-shelled molluscan debris, some crinoid ossicles and ferrigenous intraclasts. **(C)** Beige to brownish, nodular limestone. **(D)** The respective microfacies **(**FU12) is a bioclastic-peloidal wacke- to packstone composed of bryozoa (near center), thin-shelled molluscan debris, crinoid ossicles and microbioclasts.

Lianglitag Formation (L1)

The first member of the Lianglitag Formation (L1) displays meter-scale calcimicrobial-algal reefs and mounds in association with thinly-bedded pellet limestone and comprises seven facies units (Table 1; Figs. 3, 7). There is a volumetric importance of low-Mg calcite > aragonite > high-Mg calcite > biogenic opal. Low-Mg calcite derives from algal pellets, micrite and a variety of calcareous algae at high number. Calcimicrobes, bryozoans, brachiopods, ostracods and trilobites are accessory. Aragonite derives from the abundant dasycladacean algae and a variety of molluscs (bivalves, gastropods). High-Mg calcite originates from crinoid ossicles; biogenic opal from siliceous sponges (demosponges). Primary porosity refers to intraparticle pores within algal reefs, shelter pores within *Halysis* mounds, residual growth pores within calcimicrobial-sponge mounds and interparticle pores of pellet limestone. Moldic porosity derived from dasycladacean algae, molluscs and sponge spicules.

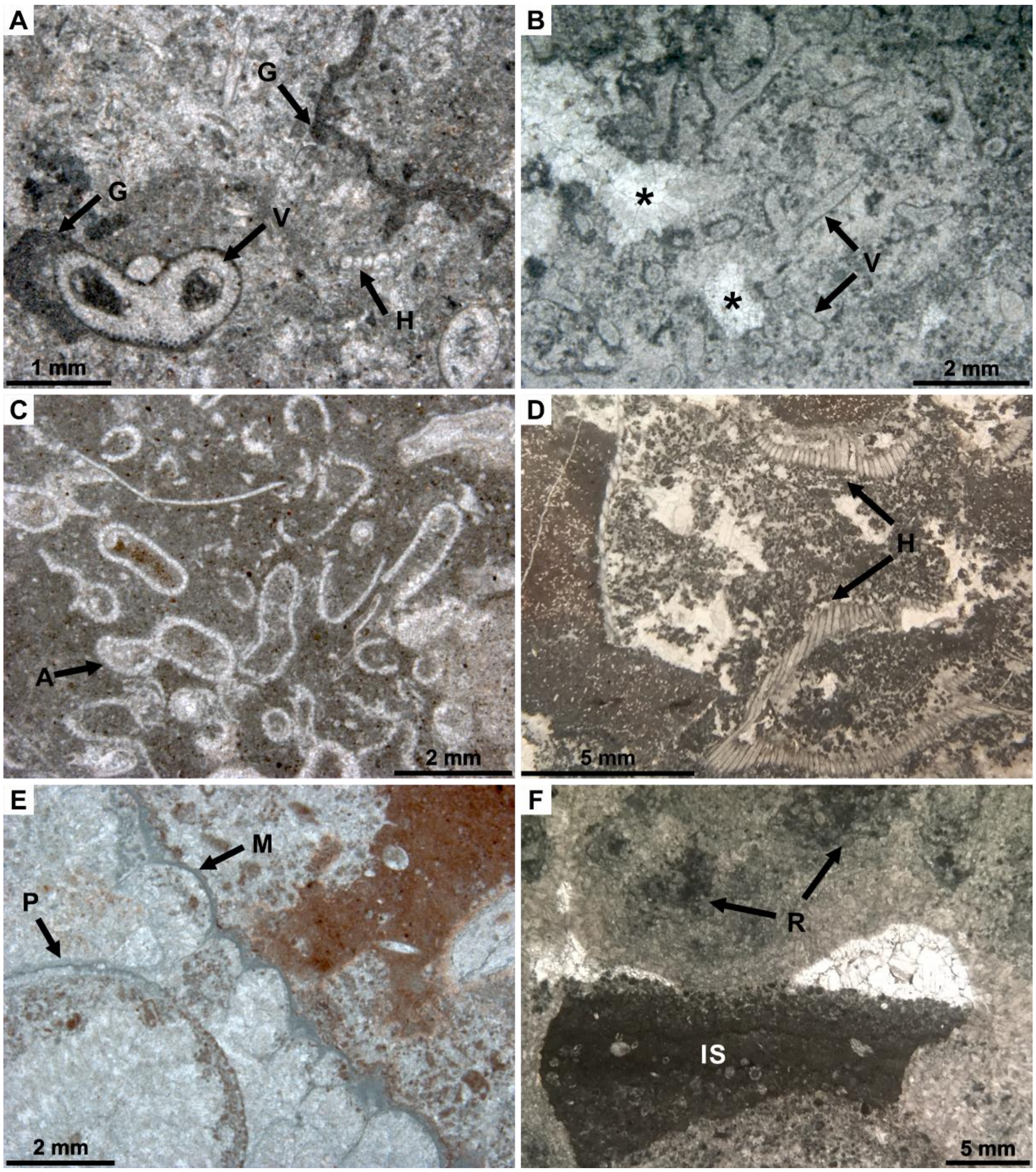

Figure—7 The first member of the Lianglitag Formation (L1), key facies units (FU), thin-sections. **(A)** FU13 is an algal-calcimicrobial boundstone, V = *Vermiporella*, G = *Girvanella*, H = *Halysis.* **(B)** FU14 is a *Vermiporella* (V) boundstone, * = centripetally cemented growth cavity. **(C)** FU15 is an *Arthroporella* (A) boundstone. **(D)** FU16 is a pellet grainstone with abundant *Halysis* (H). **(E)** FU18 is a *Palaeoporella* (P) boundstone, M = *Mastopora.* **(F)** FU19 is a calcimicrobial-sponge boundstone, R = *Renalcis*, IS = infiltrated sediment.

Lianglitag Formation (L2)

The second member of the Lianglitag Formation (L2) is an intercalation of red to grey, massive to bedded pelsparite, oncolite, oolite and fenestral biolaminite and comprises six facies units (Table 1; Figs. 3, 8). There is a volumetric importance of low-Mg calcite > aragonite. Low-Mg calcite derives from non-skeletal particles (pellets, ooids, oncoids, aggregate grains and intraclasts) and the skeletons of calcimicrobes, trilobites and ostracods. Aragonite derives from dasycladacean algae and a variety of molluscs (gastropods, bivalves). Primary porosity relates to interparticle pores in grainstone (pelsparite, oncolite, oolite) and fenestral pores present in pack- to grainstone and ooid-rich biolaminite. Early secondary porosity essentially relates to molds of aragonitic skeletons of dasycladacean algae and molluscs, locally a vuggy porosity developed.

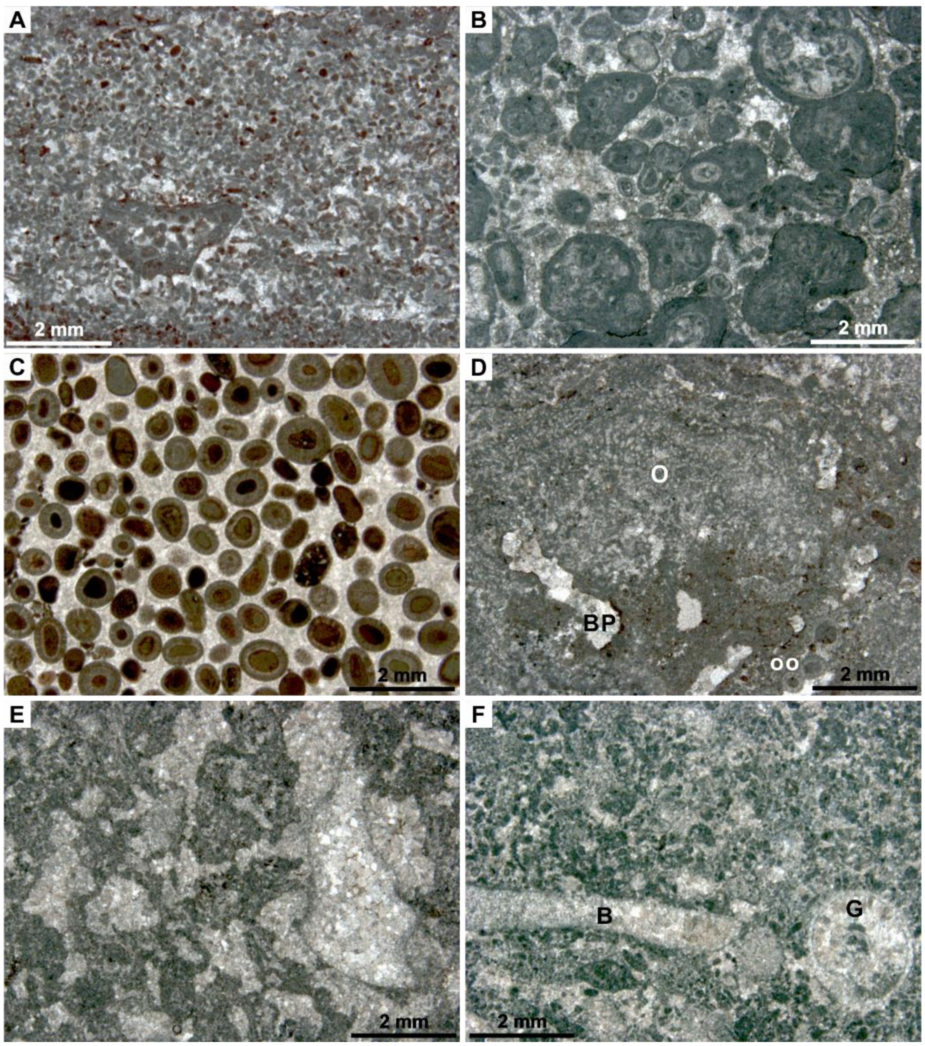

Figure—8 The second member of the Lianglitag Formation (L2), key facies units (FU), thin-sections. **(A)** FU20 is a nodular to massive pellet grainstone, note grapestone (lower left). **(B)** FU21 is an oncoid grainstone. **(C)** FU22 is an ooid grainstone. **(D)** FU23 is a nodular oolitic calcimicrobial bindstone, O = *Ortonella*, oo = ooid, BP = dissolution enhanced bird's eye. **(E)** FU24 is a cryptalgal peloid pack- to grainstone with abundant fenestrae and keystone vugs. **(F)** FU25 is an intraclastic grainstone; B = bivalve shell, G = gastropod shell.

The Diagenetic Record

The identification of diagenetic units is based on cementation and replacement phases (in the sense of dissolution-reprecipitation processes; Ca-carbonate, dolomite, silica, sulfide) in combination with phenomena such as pressure dissolution, corrosion, fracturing and hydrocarbon migration. Taken together, there are four diagenetic units, which are congruent with the four depositional units described above. The Yijianfang diagenetic unit serves as a baseline and is described in detail (Figs. 9-11). The other diagenetic units are documented in terms of their distinguishing attributes.

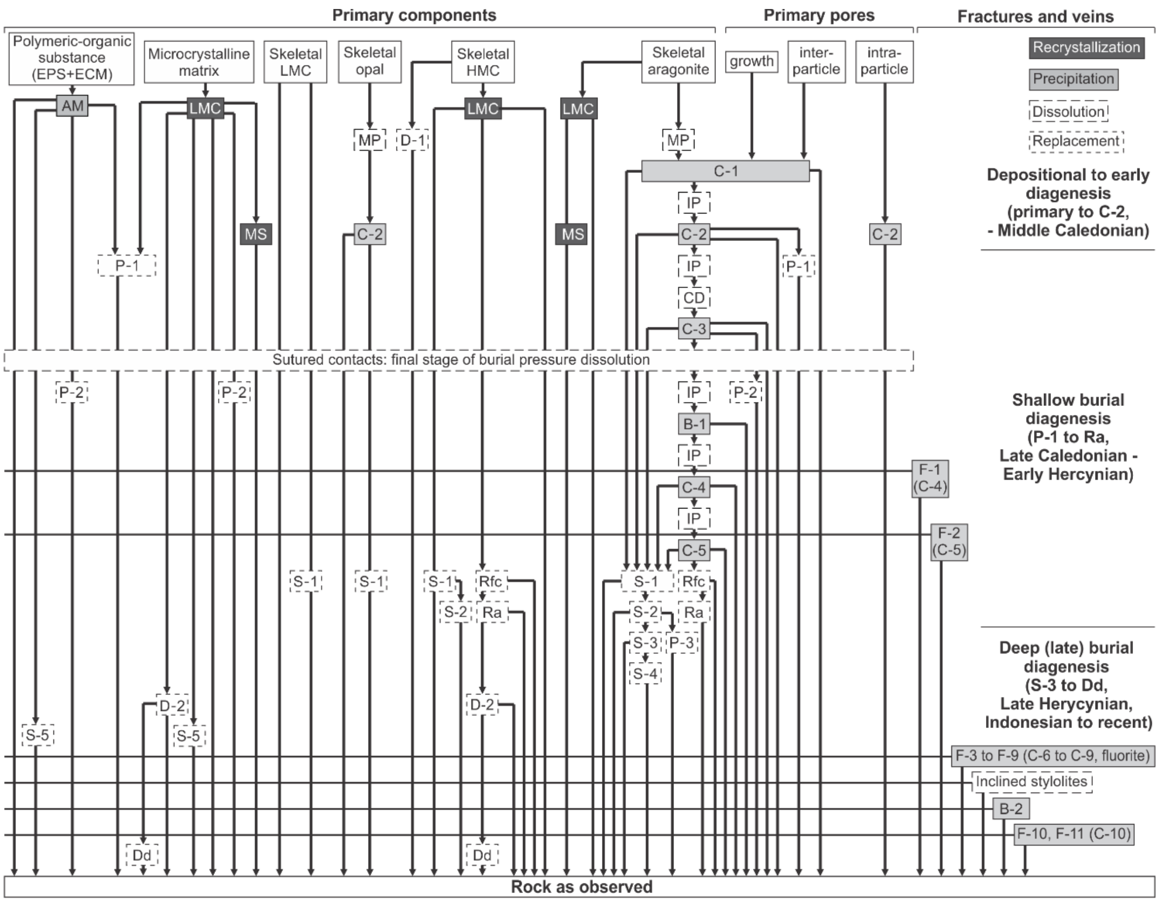

Figure—9 Petrogenetogram of the Yijianfang Formation. EPS = extracellular polymeric substances; ECM = extracellular collagenous matrix; AM = automicrite; MP = moldic pore; IP = intercrystalline pore; MS = microspar; CD = corrosion-dissolution; Rfc = replacement by ferroan calcite; Ra = replacement by ankerite; Dd = dedolomite.

Yijianfang Formation

The Yijianfang diagenetic unit (Figs. 9-11) displays ten generations of carbonate cement and thirteen replacement phases (dolomite, ankerite, calcite, silica, pyrite). Other phenomena comprise corrosion, pressure dissolution and hydrocarbon migration.

Cement fabrics: Cement-1 (C-1) is an inclusion-rich, fibrous-radiaxial calcite (non-ferroan, non-luminescent marine cement) that forms thin isopachous rims within both interparticle pores of encrinites and moldic pores of calathid sponges (Fig. 10). C-2 is an inclusion-poor, equant calcite (non-ferroan, non-luminescent) that typically forms an epitaxial overgrowth fabric upon ossicles (Fig. 10A). The calcite matrix has recrystallized to become microspar. C-3 is an inclusion-poor to limpid drusy calcite spar (Fig. 10). This phase is non-ferroan with zones of dull, orange to bright-red luminescence. C-3 occludes moldic pores (calathids, molluscs), is present in residual growth pores of sponge mounds and in residual interparticle pores of encrinites. C-4 consists of euhedral, limpid ferroan calcite with some blotchy non-ferroan intervals (Fig. 10B-D). This phase displays a poorly zoned, dull to red luminescence. C-4 represents a first generation of fracture-filling cement. C-5 is a limpid ferroan calcite phase composed of relatively large, xenomorphic crystals (mosaic) with dull to red luminescence that is generally less intense compared to C-4 (Fig. 10B-D). C-5 locally occludes residual primary and early secondary porosity. C-5 is also present as a second generation of fracture-filling cement. C-6 is a limpid calcite mosaic cementing fracture-3 and fracture-4. C-7 is a calcite microspar confined to fracture-5; C-8 a drusy ferroan calcite confined to fracture-6 and 7; C-9 is an ankerite specific to fracture-8, and C-10 is a ferroan calcite present in fracture-10 and 11.

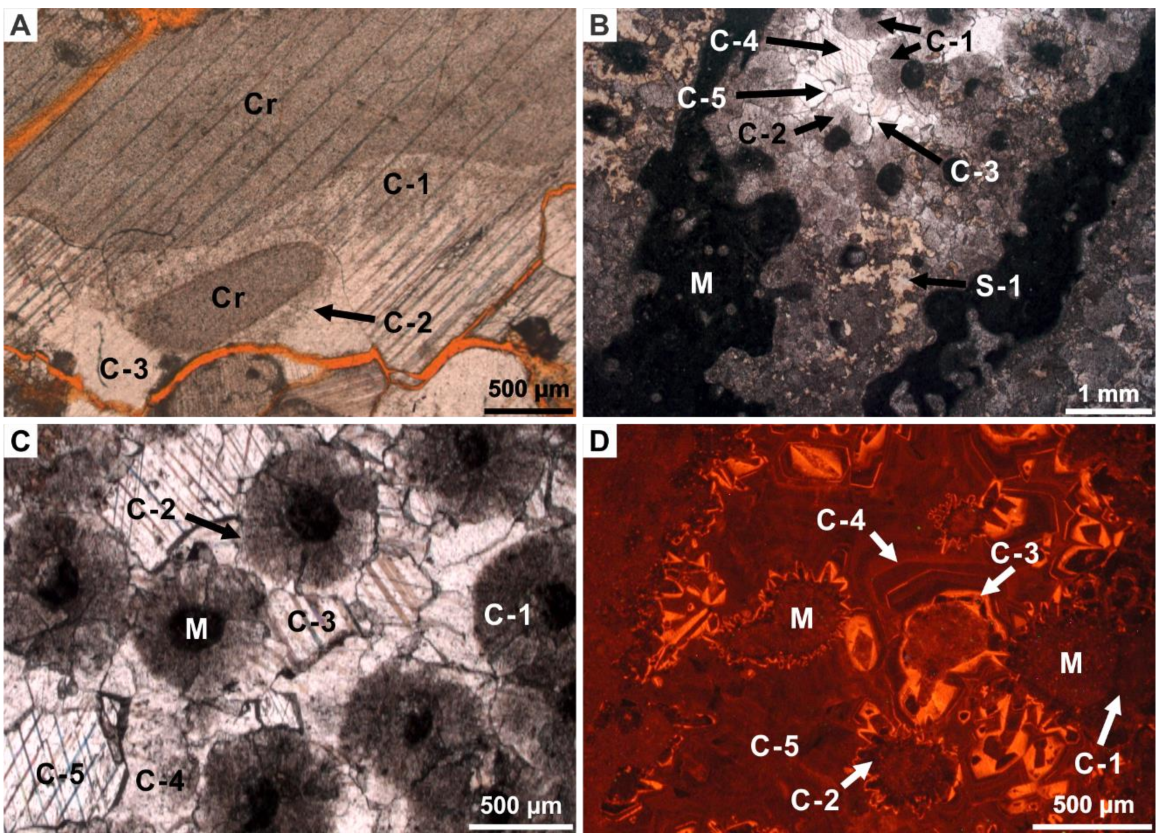

Figure—10 Diagenesis of the Yijianfang Formation, thin-section petrography: Cementation. **(A)** Cement generations (C-1 to C-3) within interparticle porosity of encrinites, normal light, Cr = crinoid fragment. **(B)** Cement generations (C-1 to C-5) within moldic porosity of a calathid sponge. Silica-1 (S-1) preferentially is replacing C-1 and C-2, M = allomicrite (infiltrated sediment), normal light. **(C-D)** Details of cement stratigraphy, C-1 to C-5, many with sutured contacts due to subsequent pressure dissolution. **(C)** normal light, **(D)** cathodoluminescence.

Replacement phases: Dolomite-1 is a microdolomite present in ossicles. Euhedral ferroan calcite replaces some calcite cements and some ossicles (Fig. 11A). This ferroan calcite is non-luminescent but displays a dark green fluorescence. Dolomite-2 consists of rhombs, about 100 µm in size, with a relatively clear center and a brownish to dark rim (Fig. 11B). It is present in ossicles and within microcrystalline matrices. Dolomite-2 displays a zoned luminescence from dull to blotchy in the center toward bright-red at outer rims. The center of dolomite-2 has a dark green fluorescence. Replacement ankerite consists of small euhedral crystals, which succeed C-5, replacement ferroan calcite and dolomite-2 (Fig. 11C). Dolomite-2 is preferentially affected by dedolomitization resulting in calcite pseudomorphs after dolomite and some Fe-(oxy)hydroxides (Fig. 11B).

There are five generations of silica that replace carbonates (Figs. 10B, 11A, C-E). Silica-1 is a yellowish crypto- to microcrystalline quartz with abundant inclusions and impurities (Figs. 10B, 11A, C). It replaces some calcite cements (C-1 to C-5) and some skeletons of bryozoa, brachiopods and crinoids. Silica-2 is a yellowish inclusion-poor phase of purported moganite (monoclinic SiO_2) with a fibrous habit under cross-polarized light (Fig. 11A). Silica-3 is a brownish chalcedony with a spherulitic habit (Fig. 11D). Silica-4 is rich in fluid inclusions and displays a mosaic habit under cross-polarized light (Fig. 11D). Ghosts of ferroan calcite, dolomite-2 and ankerite are locally present within Silica-4. Silica-5 is authigenic microquartz that is locally abundant within microcrystalline matrices (Fig. 11E). In addition, there is replacing pyrite. Pyrite-1 corresponds to framboidal aggregates partially replacing C-2 or found disseminated within microcrystalline matrices. Pyrite-2 is cubic and tens of µm in size (Fig. 11F). It partially replaces C-1, C-2 and sedimentary matrices. Pyrite-3 is cubic and hundreds of µm in size. It occurs in association with silica-2.

Other features: A corrosive micro-hiatus is present between C-2 and C-3 (Fig. 10B, C). Pyrite-2 is associated with subhorizontal pressure dissolution seams (Fig. 11F). Bitumen-1 is present in residual porosity after C-3 (Fig. 11G). Bitumen-2 occurs in association with inclined pressure dissolution seams and fracture-9. Very locally, there is fluorite in association with fracture-9 and bitumen-2 (Fig. 11H). The bitumen-2 displays a bright yellow fluorescence (Fig. 11H).

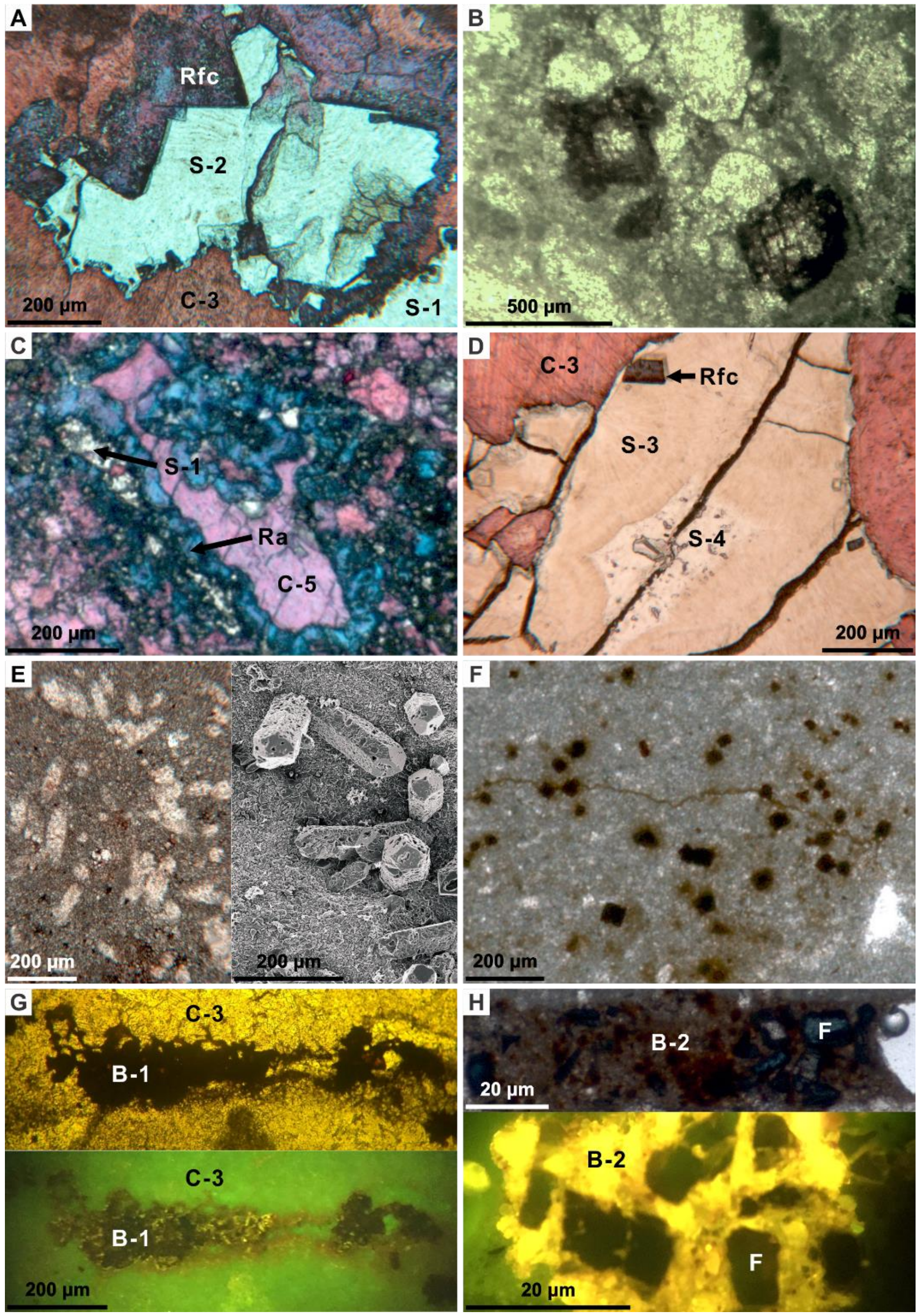

Figure—11 Diagenesis of the Yijianfang Formation, thin-section and SEM petrography: Replacement phases and other features. **(A)** Ferroan calcite (Rfc) replacing C-3 in association with replacement by silica-1 (S-1) and silica-2 (S-2) within a residual growth cavity of a calathid-demosponge carbonate mound, stained. **(B)** Matrix replacing dolomite-2 affected by calcitization (dedolomite and Fe-(oxy)hydroxides), normal light. **(C)** Ankerite (Ra) and S-1 replacing C-5 within former mold of a calathid sponge, stained. **(D)** Silica-3 (S-3) and silica-4 (S-4) in combination with Rfc replacing C-3 in a residual growth cavity of a calathid-demosponge carbonate mound, stained. **(E)** Silica-5 (S-5, authigenic microquartz) replacing microcrystalline matrix, normal light (left) and SEM micrograph (right). **(F)** Pyrite-2 (P-2) replacing sedimentary matrix in association with subhorizontal pressure dissolution seams, normal light. **(G)** Bitumen-1 (B-1) in residual porosity subsequent to C-3, normal light (upper) and fluorescence (lower). **(H)** Fluorite (F) occurring in association with F-9 and bitumen-2 (B-2), normal light (upper) and fluorescence (lower).

Tumuxiuke Formation

The Tumuxiuke diagenetic unit (Figs. 12, 14) displays several distinguishing attributes in comparison with the Yijianfang diagenetic unit described above. Here, C-1 (marine cement) is the exception, and there are only three phases of replacement carbonate (dolomite-1, -2; calcite pseudomorphs after dolomite-2). There is disseminated hematite (Fig. 14A). Bitumen-1 and -2 occur in the same context as in the Yijianfang Formation, but some bitumen-1 also migrated into the intercrystalline porosity confined by C-4 (Fig. 14B).

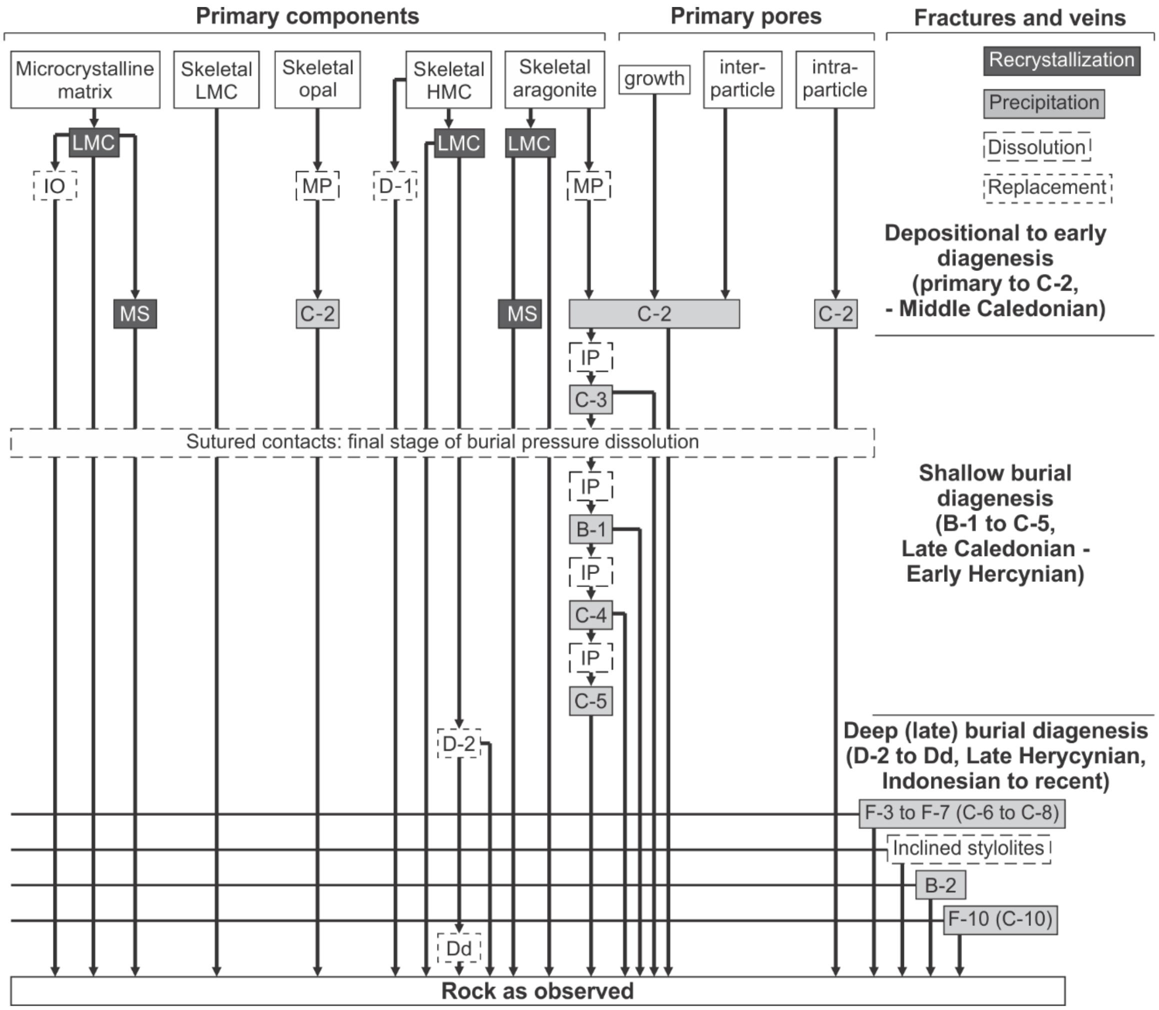

Figure—12 Petrogenetogram the Tumuxiuke Formation. See Fig. 8 for legend; IO = iron oxides.

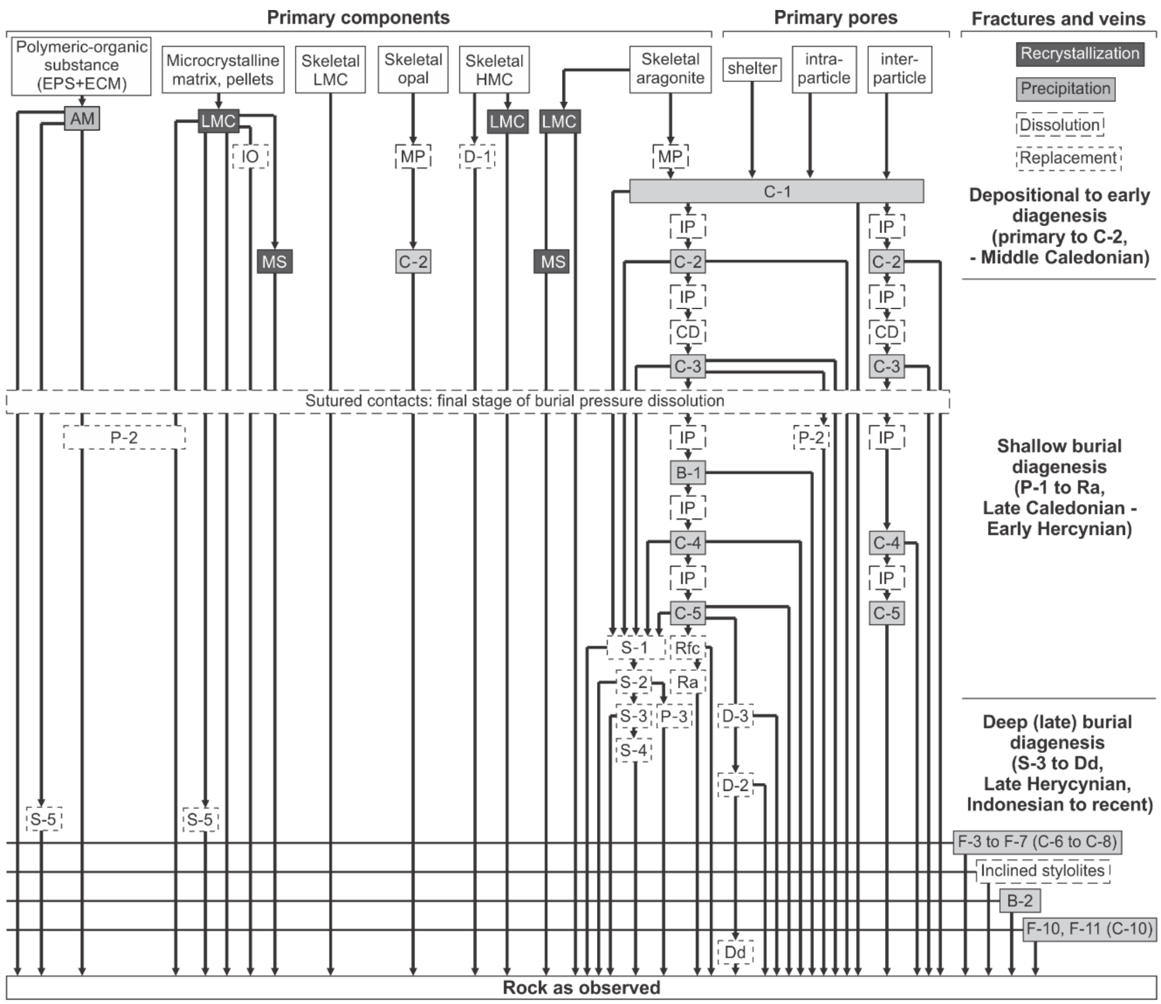

Figure—13 Petrogenetogram of the first member of the Lianglitag Formation (L1). See Fig. 8 for legend.

Lianglitag Formation (L1)

For the Lianglitag (L1) diagenetic unit (Figs. 13, 14) in comparison with the Yijianfang Formation, phase C-1 (marine cement) is much more important and occluded more efficiently inter- and intraparticle porosity as well as growth cavities and moldic porosity (Fig. 14C-E). C-1 locally displays a dull red luminescence and is fluorescent. C-2 grades into a limpid, fibrous to bladed calcite with a dull-red luminescence that by itself grades into a drusy to blocky calcite mosaic with a dull-red luminescence (Fig. 14F). This unit hosts an additional replacing dolomite-3. These are mm-size crystals with a non-ferroan, non-luminescent center and a ferroan, bright-orange luminescent rim (Fig. 14G, H). Dolomite-3 occurs in calcite-cemented molds and intraparticle pores of calcareous algae. It preferentially replaces cements-3 to -5. Some bitumen-1 is present in the intercrystalline porosity confined by C-4, C-5 and dolomite-3 (Fig. 14G, H).

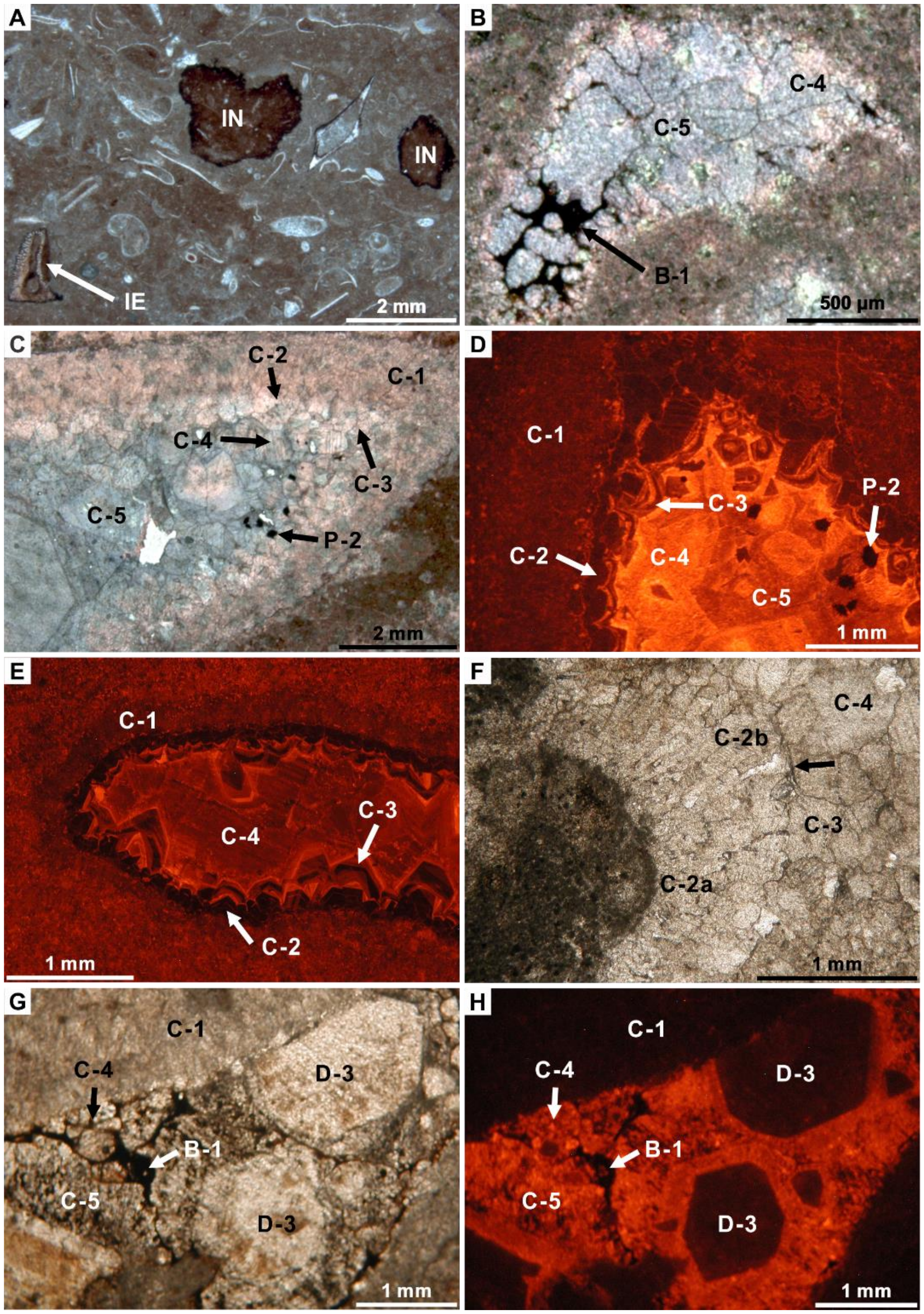

Figure—14 Diagenesis of the Tumuxiuke (**A**, **B**) and the Lianglitag (L1) formations (**C** to **H**); thin-sections: **(A)** Cemented molds of thin-shelled molluscan debris, disseminated hematite, iron-oxide coated grains (IE) and intraclasts with ferrigenous oncoidal envelopes (IN), normal light. **(B)** Bitumen-1 (B-1) within dissolution-enhanced, intercrystalline porosity defined by C-4 and C-5, stained. (**C-D**) Cement generations C-1 to C-5 and replacement pryite-2 (P-2) within a former moldic pore of *Palaeoporella*; **(C)** stained, **(D)** cathodoluminescence. **(E)** Cement generations C-1 to C-4 within a growth pore adjacent to a siliceous sponge, cathodoluminescence. **(F)** A succession of cement-2 (C-2a, C-2b) to cement-4 within a moldic pore of a dasycladacean alga. There is corrosion (microhiatus) between C-2 and C-3 (arrow). **(G-H)** Dolomite-3 (D-3) replaced cement-4 (C-4) and cement-5 (C-5) within intraparticle porosity of a dasycladacean alga. Bitumen-1 (B-1) is present in the dissolution-enhanced intercrystalline pores of C-4 and C-5. **(G)** normal light, **(H)** cathodoluminescence.

Lianglitag Formation (L2)

For the diagenetic unit L2 (Figs. 15, 16) in comparison with the Yijianfang Formation, phase C-1 (marine cement) is equally or even more important (Fig. 16A-C). In addition, locally there is a limpid dog-tooth calcite cement associated with internal sediment (Fig. 16E) indicating episodes of freshwater diagenesis. This cement is non-ferroan, blotchy-dull luminescent to non-luminescent and may occur in interparticle porosity as well as in fenestral and moldic pores. Erosion surfaces (subhorizontal corrosion) are present in some oolites (Fig. 16F). There is a specific matrix-replacing dolomite-4. It is composed of submillimeter-size crystals with a dull-luminescent center and a bright orange rim with yellow to light orange fluorescence (Fig. 16G-H). Dolomite-4 preferentially replaces pellets. Some bitumen-1 migrated into the intercrystalline porosity of dolomite-3 (Fig. 16I).

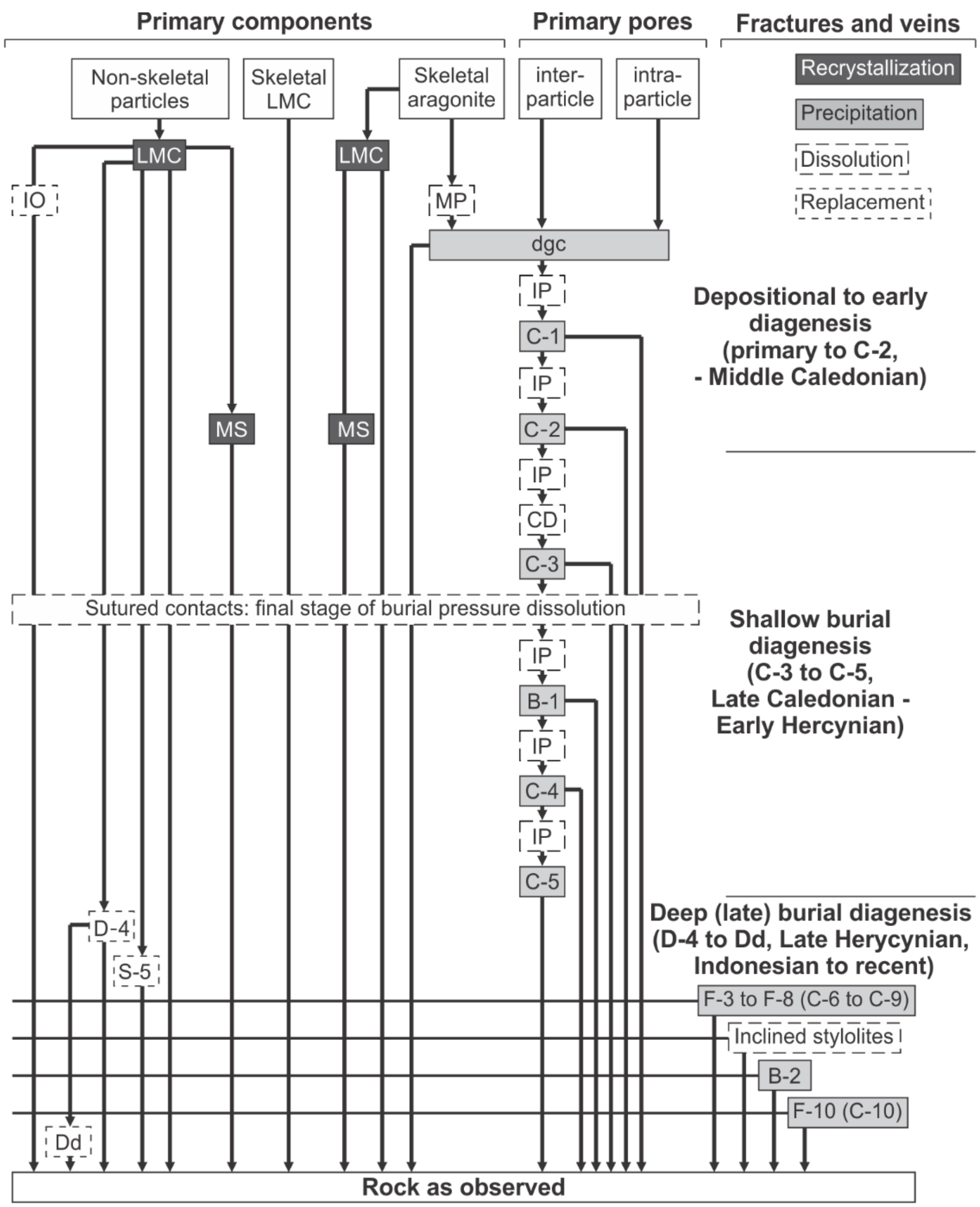

Figure—15 Petrogenetogram of the second member of the Lianglitag Formation (L2). See Fig. 8 for legend. dgc = dog-tooth calcite cement.

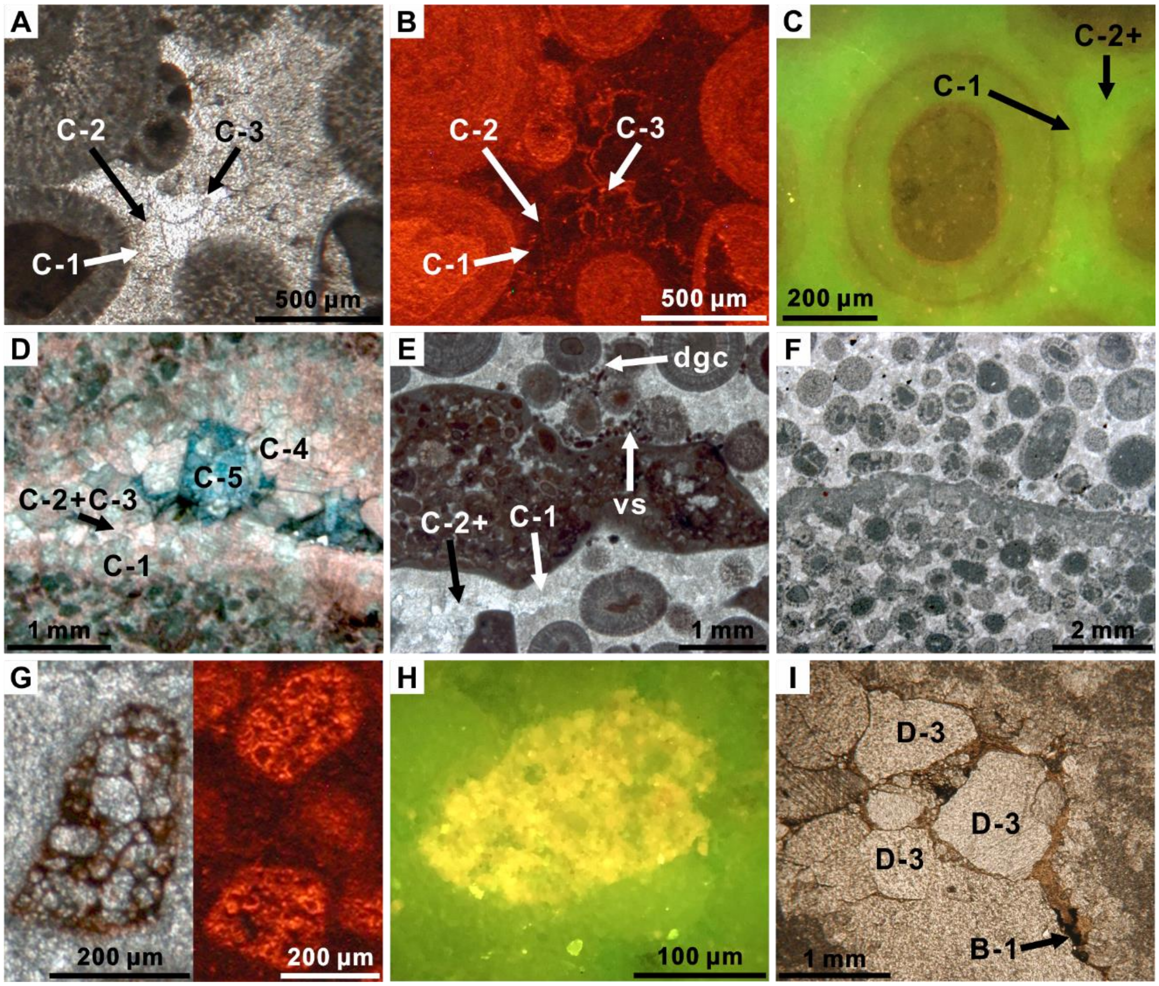

Figure—16 Diagenesis of the second member of the Lianglitag Formation (L2), thin-sections: **(A-C)** Early generations of cement (C1 to C-3) present in oolites (o), **(A)** normal light; **(B)** cathodoluminescence; **(C)** fluorescence. **(D)** Succession of C1 to C-5 occluding moldic porosity, stained. **(E)** Local occurrence of limpid dog-tooth cement (dgc) associated with vadose silt (vs) succeeded by isopachous rims of C-1, normal light. **(F)** Oolite with discontinuity due to erosion, corrosion and subhorizontal dissolution, normal light. **(G-H)** Dolomite-4 (D-4) as replacement of microcrystalline algal pellets in a peloidal grain- to packstone; **(G)** normal light (left), cathodoluminescence (right), **(H)** fluorescence. **(I)** Bitumen-1 (B-1) related to an intercrystalline porosity associated with dolomite-3 (D-3), normal light.

The Carbon and Oxygen Isotope Record

The cross-plot of the full data set of component-specific carbon- and oxygen-isotope values (Fig. 17; Table 2; supplementary data file) displays a broad scatter of $\delta^{18}O$ values (min = -11.2, max = -3.0, mean = -6.4 ‰, σ = 1.7). The scatter follows a trend of decreasing $\delta^{18}O$ values along with progressing diagenesis in both the Yijianfang and the Lianglitag formations. There are three hierarchically distinct levels along which $\delta^{13}C$ values are plotting (Fig. 17) thereby distinguishing three stratiform C-isotope geochemical segments congruent with the Yijianfang, the Tumuxiuke and the Lianglitag formations (L1+L2).

The Yijianfang Formation is characterized by relatively low $\delta^{13}C$ values (n = 52, median = 0.6 ‰, min = -0.4 ‰, max = 1.0 ‰). There are five clusters in this data set tagged as Y-a to Y-e (Fig. 17, Table 2). The Tumuxiuke Formation (own data and those of Zhang & Munnecke, 2016) represents $\delta^{13}C$ values exclusively obtained from the reddish microcrystalline matrix. It displays intermediate $\delta^{13}C$ values (n = 14, median = 1.3 ‰, min = 0.8 ‰, max = 1.7 ‰). The Lianglitag Formation is characterized by ^{13}C-enriched values (n = 107, median = 2.6 ‰, min = 1.8 ‰, max = 3.2 ‰). There are five clusters tagged as L-a to L-e. Comparing most positive values of cluster Y-a with those of cluster L-a, there is a generalized $\Delta^{13}C_{carbonate}$ reaching up to +2.5 and a respective $\Delta^{18}O_{carbonate}$ reaching up to +2.0 (Fig. 17).

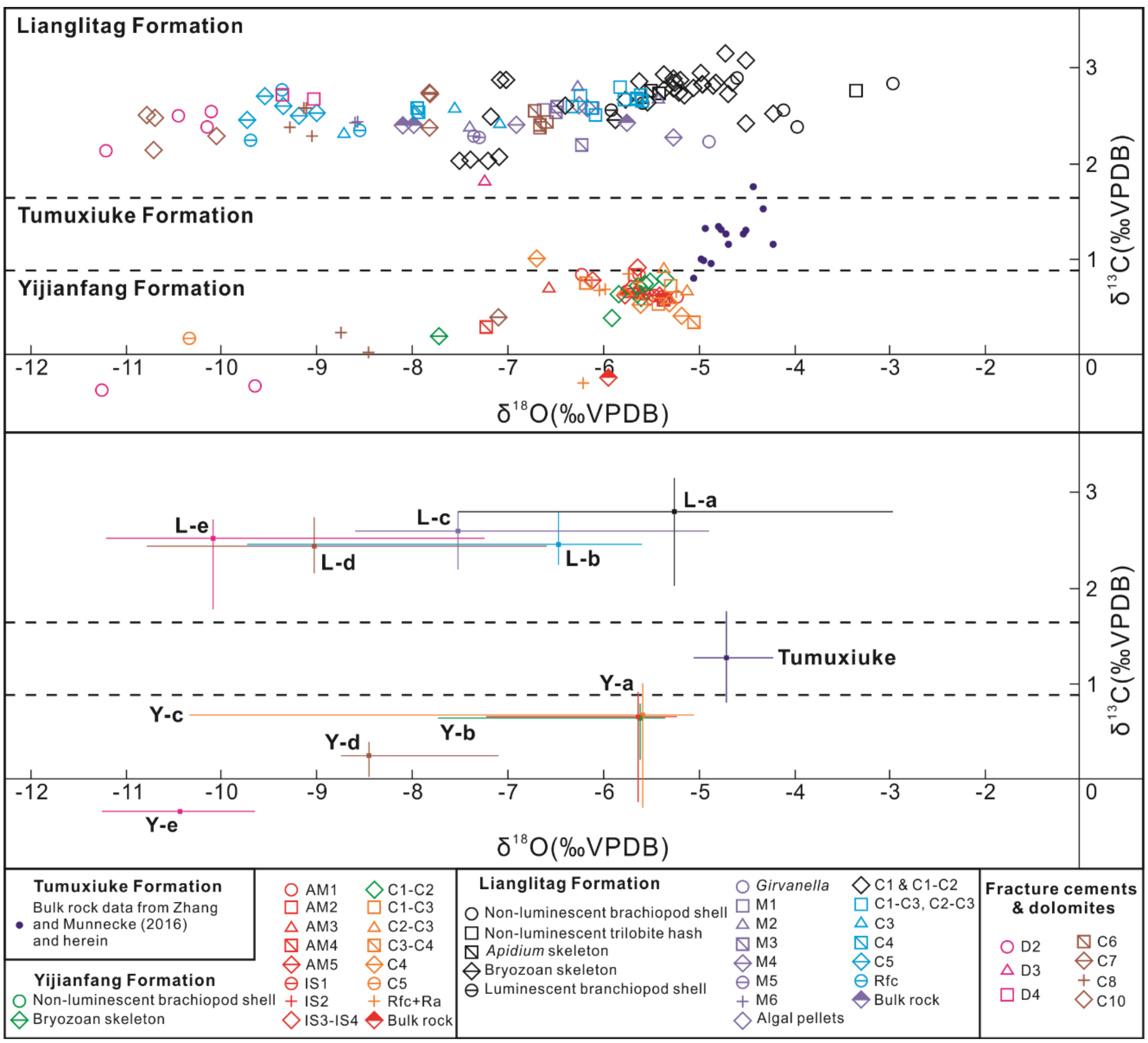

Figure—17 Cross-plot of component-specific values of carbon and oxygen stable isotopic composition defining three isotope geochemical segments across the Middle to Late Ordovician, Bachu Uplift, northwestern Tarim Basin. See Table 2 for details.

Table—2 Geochemical segments and respective sets of carbon and oxygen stable isotope values ($\delta^{13}C$, $\delta^{18}O$ in ‰ VPDB) present in the Middle to Late Ordovician succession at Bachu Uplift, western Tarim Basin, Bachu (Maralbexi) county, Xinjiang Uyghur Autonomous Region, NW China (see also Fig. 17).

Geochemical segment/ cluster	**Number of samples**	**$\delta^{13}C$ (‰)**				**$\delta^{18}O$ (‰)**				**Carbonate components**
		min	**max**	**mean**	**median**	**min**	**max**	**mean**	**median**	
Yijianfang F.	52	-0.4	1.0	0.6	0.6	-11.2	-5.0	-6.1	-5.6	All samples of Yijianfang Formation
Y-a	10	0.2	0.8	0.6	0.6	-7.7	-5.3	-5.8	-5.6	LMC of brachiopods, bryozoans and early cements C-1 and C-2
Y-b	20	0.3	0.9	0.7	0.6	-7.2	-5.2	-5.8	-5.6	Microcrystalline matrix and peloids
Y-c	17	-0.3	1.0	0.6	0.7	-10.3	-5.0	-5.9	-5.6	Cement C-3, C-4, C-5; replacement phases ferroan calcite and ankerite
Y-d	3	0.0	0.4	0.2	0.2	-8.8	-7.1	-8.1	-8.5	Fracture-filling cement C-7 and C-8
Y-e	2	-0.4	-0.3	-0.3	-0.3	-11.2	-9.6	-10.4	-10.4	Replacement phase dolomite-2
Tumuxiuke F.	14	0.8	1.7	1.2	1.3	-5.0	-4.2	-4.7	-4.7	Microcrystalline matrix of red nodular limestone (Tumuxiuke Formation)
Lianglitag F.	107	1.8	3.2	2.6	2.6	-11.2	-3.0	-6.8	-6.4	All samples of Lianglitag Formation
L-a	42	2.0	3.2	2.7	2.8	-7.5	-3.0	-5.4	-5.2	LMC of brachiopods, bryozoans, trilobites, *Apidium*, cements C-1 and C-2
L-b	21	2.2	2.8	2.5	2.4	-8.6	-4.9	-6.7	-6.5	Peloids and bulk rock samples
L-c	23	2.2	2.8	2.6	2.6	-9.7	-5.6	-7.5	-7.5	Cements C-3, C-4, C-5; replacement phase ferroan calcite
L-d	15	2.1	2.7	2.5	2.4	-10.8	-6.6	-8.6	-9.0	Fracture-filling cement C-6, C-7, C-8 and C-10
L-e	7	1.8	2.7	2.4	2.5	-11.2	-7.2	-9.6	-10.1	Replacement phase dolomite-2, -3 and -4
Summary	173	-0.4	3.2	1.9	2.4	-11.3	-3.0	-6.4	-5.8	All samples

Integrating Component-Specific and Bulk Geochemical Data

The calculated values of virtual bulk samples (Fig. 18) are bracketed by values typical for an early marine (high values) and a late burial diagenetic origin (low values). The Tumuxiuke Formation is an exception because component-specific data do not exist, that is, only Gaussian scattering is displayed. Figure 18 serves as an example of the complexity of fluid-carbonate alteration along burial pathways and the related exchange and recalibration of isotope values (Swart, 2015; Müller *et al*., 2020; Fantle *et al*., 2020). As expected, the bulk-geochemical values of carbonates are often much more sensitive to alteration with regard to $\delta^{18}O$ (due to the large volume of oxygen in the fluid reservoir) than for $\delta^{13}C$ values (due to the large volume of carbon in the rock reservoir; Veizer *et al*. 1999). In addition, the impact of ^{13}C-depleted values during burial appears more significant for the Yijianfang than for the Lianglitag Formation. For the Yijianfang Formation, the intrinsic error of bulk geochemical samples (mean, 3σ) is assessed at 0.5 ‰ ±0.5 for $\delta^{13}C$ and at -6.5 ‰ ±1.5 for $\delta^{18}O$. In the Tumuxiuke Formation, the intrinsic error is at 1.2 ‰ ±0.6 for $\delta^{13}C$ and at -4.6 ‰ ±0.6 for $\delta^{18}O$. For the Lianglitag Formation, the error is at 2.5 ‰ ±0.5 for $\delta^{13}C$ and at -7.1 ‰ ±2.8 for $\delta^{18}O$.

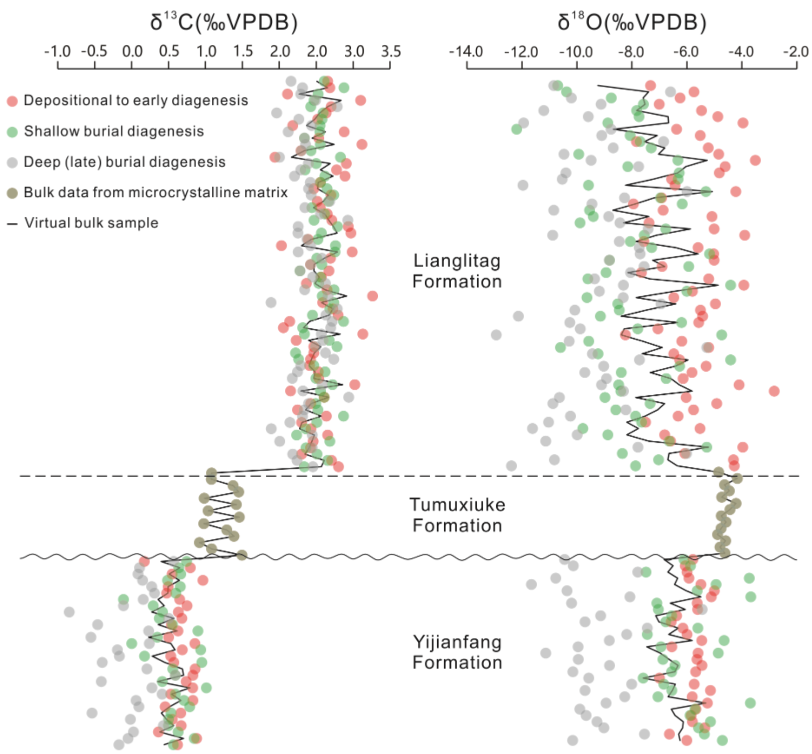

Figure—18 Carbon and oxygen isotopic values of virtual bulk samples (black line) at the formation scale. For the Tumuxiuke Formation only Gaussian scattering is displayed. Note that ^{13}C-depleted values during burial appear more significant for the Yijianfang than for the Lianglitag Formation. For the Yijianfang Formation, the intrinsic error of bulk geochemical samples (mean, 3σ) is at 0.5 ‰ ±0.5 for $\delta^{13}C$ and at -6.5 ‰ ±1.5 for $\delta^{18}O$. For the Tumuxiuke Formation, the intrinsic error is at 1.2 ‰ ±0.6 for $\delta^{13}C$ and at -4.6 ‰ ±0.6 for $\delta^{18}O$. For the Lianglitag Formation, the error is at 2.5 ‰ ±0.5 for $\delta^{13}C$ and at -7.1 ‰ ±2.8 for $\delta^{18}O$. By consequence, bulk geochemical samples cannot resolve $\delta^{13}C$ anomalies ≤ 1 ‰-points. For $\delta^{18}O$ values, careful data filtering is required and mainly smoothed long-term trends should be considered.

INTERPRETATION AND DISCUSSION

Prelude

In the Ordovician of the Leyayilitag region, there is a succession of four depositional units, which represent both environmental change (different ramp to platform settings as deduced from facies and rock textures) and substantial biodiversification (calcareous algae, calcimicrobes) going along with increasing importance of reefal framework construction and depositional aragonite. There are four congruent diagenetic units that host a large variety of secondary chemical precipitates (by number and volume) thereby constraining the informative value of the published bulk-rock $\delta^{13}C$ and $\delta^{18}O$ data-set. A scatter plot of component-specific values discriminates three generalized chemostratigraphic segments, but caution and data filtering are required in order to establish an integrated chronostratigraphic record of carbon- and oxygen isotopes at regional scale of the Middle to Late Ordovician of the western Tarim Basin.

The Depositional Record: Setting the Stage

Ordovician biodiversity and relative sea-level reach their acme around the Sandbian-Katian boundary interval, roughly coincident with the GICE (Rasmussen *et al*., 2019). In the Tarim Basin this global trend is expressed, for example, by the nature of carbonate buildups which evolved from microbial mounds to skeletal framework reefs *via* calathid-demosponge carbonate mounds and calcimicrobial-algal reef mounds (Jiao *et al*., 2011; Wang *et al*., 2012; Zhang *et al*., 2014a; Shen & Neuweiler, 2015, 2018; Shi *et al*., 2016). An additional pulse of biodiversification occurred during the early Katian as exemplified by calcimicrobes and calcareous algae (Riding & Fan, 2001; Shen & Neuweiler, 2016; Liu *et al*., 2020). This regional expression of a global trend leads to a profound contrast between the Yijianfang and Lianglitag formations in terms of community structure, texture and primary mineralogy. The Yijianfang Formation represents a benthic community dominated by active filter feeders and passive suspension feeders (calathid and siliceous sponges, pelmatozoans), minor growth frameworks and an essentially calcitic mineralogy (Wang *et al*., 2017a; Li *et al*., 2017; Shen & Neuweiler, 2018). By contrast, the Lianglitag Formation is dominated by primary producers, reefal fabrics and a substantial increase of aragonite due to the boosting dasycladacean algae (Zhang *et al*., 2014a; Shen & Neuweiler, 2016). The overall pattern and timing are in accord with GOBE (Webby, 2004), thus being largely independent of changes of relative sea-level and associated shifts of facies.

At regional scale, the history of the sponge-pelmatozoan consortium of the Yijianfang Formation deserves special attention. The major hiatus that succeeds the Yijianfang Formation, although perennially advocated as such (Hu *et al*., 2014; Liao *et al*., 2016), is not straightforwardly related to uplift, subaerial exposure and subsequent karstification. Instead, its locally developed cavernous secondary porosity (forming significant hydrocarbon reservoirs) is due to deep burial dissolution associated with fractures and pulses of corrosive fluids ahead of migrating hydrocarbons (Baqués *et al*., 2020). Instead, there is an accord with Wang *et al*. (2017b, 2019), considering the top of the Yijianfang Formation an (environmental) drowning unconformity (Schlager, 1999). Because there is no depositional or textural evidence for a current-swept structural high (Fig. 5, FU-10 in Table 1), an ecological demise of the Yijianfang shallow-water carbonate factory appears likely thereby reaching well beyond a singular extinction of calathid sponges. The uniformly small-size crinoid ossicles present in the uppermost part of the Yijianfang Formation (Fig. 5; FU 10 in Table 1) suggest biotic response to environmental stress. Crinoid dwarfism reported from the end-Ordovician biotic crises (Borths & Ausich, 2011) might serve as an analogy. In the present-day oceans, echinoderm dwarfism occurs in connection with a disturbed life cycle due to acidification (Hennige *et al*., 2014).

The highly heterogeneous depositional record sets up the stage for both early diagenetic reactivity of the host carbonates and the geologically preserved $\delta^{13}C$ record. In terms of their depositional to early post-depositional fluid conductivity, the Tumuxiuke Formation and the second member (L2) of the Lianglitag Formation acted as fluid bafflers. For the Tumuxiuke Formation, this is due to the low permeability of microcrystalline limestone; for L2, this is due to the low permeability of both fenestral limestone and pervasively cemented oolite. In terms of the initial $\delta^{13}C$ record, the bahamite-type deposits of the Lianglitag Formation represent the most productive carbonate factory in scope. There is also an uneven distribution of both calcareous algae (vital effect, photosynthesis; cf. Geyman & Maloof, 2019) and the initial amount of aragonite with its distinct carbon isotope fractionation factor (Swart, 2008; Lécuyer *et al*., 2012).

Assessing the Impact of Diagenetic Alteration

During burial, the initial layer-cake character of the succession became even more distinct. Indeed, the products of diagenesis in the Yijianfang Formation and the first member (L1) of the Lianglitag Formation are rather similar and record confined fluid flow. The fluid baffling Tumuxiuke Formation appears relatively inert, only displaying matrix recrystallization, some cemented molds and replacement dolomite. Fluid baffler L2 is specific in terms of the importance of early cementation (marine-phreatic C-1, episodes of freshwater diagenesis) and late dolomitization (dolomite-3 and -4). Early phases of replacing silica in the Yijianfang Formation and in L1 likely are local in origin (Cui *et al*., 2012; Bjørlykke & Jahren, 2012; Neuweiler *et al*., 2014; Chen *et al*., 2020). The congruent layer-cake pattern suggests no major resetting due to, i.e., thermobaric dolomitization, hydrothermal alteration or major fracturing in this part of the Tarim Basin (Jiang *et al*., 2014), instead a stratiform rock-buffered diagenetic system prevailed (cf. Czerniakowski *et al*., 1984; Moore, 2001; Bjørlykke & Jahren, 2012; Christ *et al*., 2018).

The generation of virtual bulk samples allows the assessment of threshold values rather typical for diagenetic alteration (Fig. 18) which, in a subsequent step, should be neglected for chemostratigraphic reconstruction. For the Yijianfang Formation, that was influenced by late diagenetic, ^{12}C –enriched, hydrocarbon-bearing fluids, this concerns values of $\delta^{13}C$ of <0.2 ‰. For the Lianglitag Formation this concerns values of $\delta^{13}C$ <1.5 ‰. For $\delta^{18}O$ a generalized threshold value of <6.0 ‰ was determined (see Fig. 18).

Chronostratigraphic Synopsis of Carbon and Oxygen Isotope Values

Figure 19 represents an effort to present a rather complete and chronostratigraphically-arranged data set of $\delta^{13}C$ and $\delta^{18}O$ values filtered from data typical for diagenetic alteration and integrating literature bulk data (Zhang & Munnecke, 2016; Liu *et al*., 2019a; Chang *et al*., 2021) at the regional scale. As a reminder, for $\delta^{13}C$ values, the bulk geochemical data set holds a potential error of up to ±0.5 ‰-points in function of depositional facies and the importance of secondary precipitates. Therefore, any short-term $\Delta^{13}C_{carbonate}$ well below 1 ‰-points is considered insignificant. For $\delta^{18}O$ values, the potential error of bulk geochemical samples is too large (up to ±2.8 ‰) to aid in any short-term or mid-term paleoenvironmental interpretation without additional evidence. Therefore, only composite and discrete baseline shifts along a smoothed long-term trend are considered.

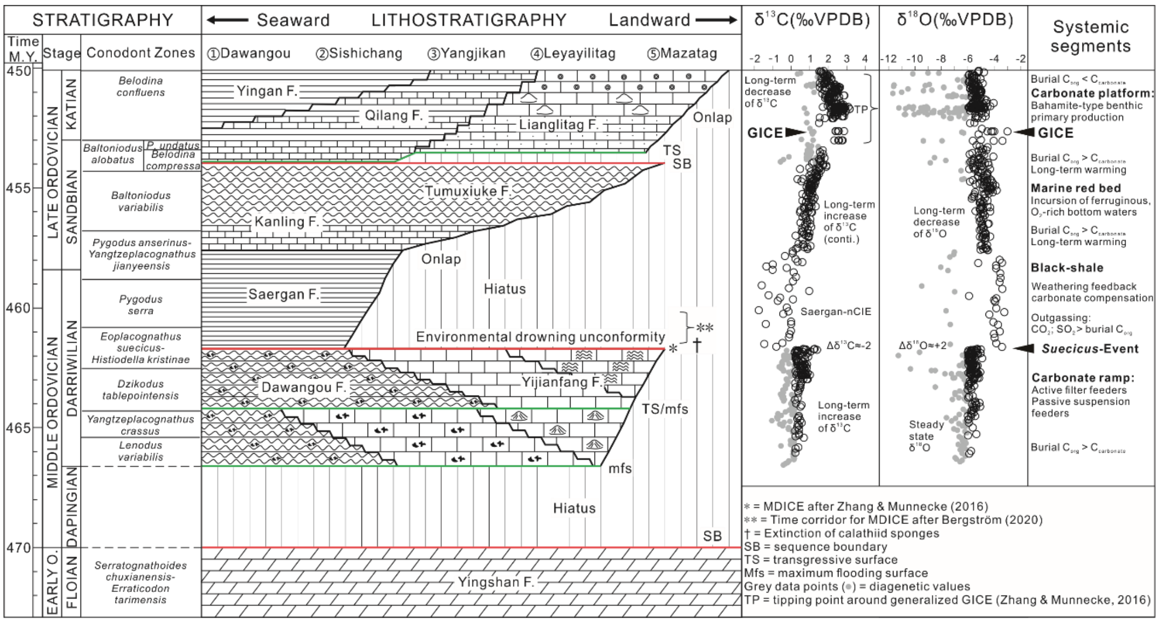

Figure—19 Synoptic compilation of chronostratigraphically-arranged $\delta^{13}C$ and $\delta^{18}O$ values across the Middle to Late Ordovician of the western Tarim Basin. There is no evidence in support of the presence of the Middle Darriwilian (positive) Isotopic Carbon Excursion (MDICE) in this region. Instead, there is an abrupt onset of the regional Saergan-nCIE (*Suecicus*-Event) associated with the demise of the Darriwilian carbonate factory. With caution, the Katian Guttenberg carbon-isotope excursion (GICE) is identified below the tipping point of long-term trends of steadily rising and steadily declining $\delta^{13}C$ values ($\delta^{13}C_{max} \approx 3.2$ ‰). It represents rapidly rising $\delta^{13}C$ values associated with a positive shift of $\delta^{18}O$ values. The GICE associated baseline shift of $\delta^{13}C$ values is interpreted to result from the development of a boosting bahamite-type Katian carbonate factory.

Long term trends

There is a long-term positive shift of $\delta^{13}C$ values starting at around 0 ‰ near the base of the succession and peaking at 3.2 ‰ recorded in early marine diagenetic cement (C-1; C-2) in *Palaeoporella* reefs (FU 18 in Table 1). This peak value plots close to the base of the early Katian *Belodina confluens* Zone. After this tipping point (TP in Fig. 19), there is a steady trend of decreasing $\delta^{13}C$ values over the remaining portion of the succession. The long-term trend of $\delta^{18}O$ values starts with steady minimum values, displays an abrupt positive shift ($\Delta^{18}O \approx +2.0$) at the base of the Saergan black-shales (Fig. 4), and then returns to low values in a generalized asymptotic fashion, though punctuated by another positive shift ($\Delta^{18}O \approx +2.0$) in the lower portion of the Lianglitag Formation. Only these positive shifts will be discussed below as they occur contemporaneously with shifting $\delta^{13}C$ values at the mid-term and short-term scale, respectively (*Suecicus*-Event and GICE of Fig. 19).

The long-term rise of $\delta^{13}C$ values appears global as it can be traced back to the Early Ordovician starting with moderately negative values (Qing & Veizer, 1994; Veizer *et al*., 1999; Shields *et al*., 2003; Bergström *et al*., 2009; Bergström, 2020). Some previous workers argued that at the time scale of a few tens-of-Myr, the principal parameter in play is the relative rate of burial of disseminated C_{org} *versus* that of $C_{carbonate}$ (Weissert *et al*., 1998; Veizer *et al*., 1999; Berner, 2003; Saltzman & Thomas, 2012). Assuming that this concept holds true, until the earliest Katian, the effect of C_{org} burial dominates that of $C_{carbonate}$ burial, and after the tipping point, this relationship is reverse. For this scenario, there is gross coincidence with the timing and extent of biodiversification (implying enhanced primary productivity and burial) of marine phytoplankton, then followed by the largest tropical shelf area in Earth's history with its associated acme of carbonate sediment production (Walker *et al*., 2002; Servais *et al*., 2009). In the Tarim Basin, the bahamite-type deposits of the Lianglitag Formation express the boosting rate of carbonate sediment production and its subsequent burial.

Medium-term segments

The Saergan Formation holds a significant interruption of the long-term trend of rising $\delta^{13}C$ (mean $\delta^{13}C$ = -0.4 ‰). This formation consists of black shale grading into black shale-limestone alternation (Fig. 4) and is considered an important hydrocarbon source rock (kerogen type II, TOC up to 5%, mean $\delta^{13}C_{org}$ = -28,5; Zhang *et al*., 2002; Ma *et al*., 2006; Chen *et al*., 2012; Huang *et al*., 2016; Berry, 2010 for review of Middle Ordovician black shales). The Saergan negative excursion (Saergan-nCIE) is centered around the Darriwilian *Pygodus serra* Zone and reaches into the earliest Sandbian. It appears to have a slightly more rapid onset than recovery with a small final overshoot (cf. Vervoort *et al*., 2019). The onset correlates with an abrupt positive shift of $\delta^{18}O$ values ($\Delta^{18}O \approx +2.0$).

This medium-term Darriwilian to earliest Sandbian negative excursion is of pronounced regional extent, at least covering the Tarim Basin and the Yangtze Platform together forming part of the Cathay-Tasman biogeographic Province of Cocks & Torsvik (2020). Searching for analogue patterns at global scale (Bergström *et al*., 2020), the Basal Dapingian Negative Isotopic Carbon Excursion (BDNICE) appears too insignificant ($\Delta^{13}C_{carbonate}$ < 1) and inappropriate (too old) in terms of chronostratigraphic age. The Lower Sandbian Negative Isotopic Carbon Excursion (LSNICE) might be an alternative but it is too short in duration, chronostratigraphically too young and of restricted (Baltoscandian) extent. Even more important, the widely identified Middle Darriwilian (positive) Isotopic Carbon Excursion (MDICE) is expected to occur in between those two negative excursions, a time corridor that is covered by the Saergan-nCIE of the western Tarim Basin (Fig. 19). The Saergan-nCIE is associated with the demise and large-scale absence of shallow-water carbonate sediment production in the Tarim Basin. Intriguingly, this peculiar configuration also applies for the Yangtze Platform. In this area, there is a major hiatus between the Shihtzupu and the Pagoda formations. Correlative conformable deposits (C_{org}-rich slope to basin deposits) hold a negative $\delta^{13}C$ excursion with the MDICE being untraceable (Huangnitang section; Munnecke *et al*., 2011). Together with its associated positive $\delta^{18}O$ anomaly, the lower part of the Saergan Formation holds a major regional event justifying a new term, the *Suecicus*-Event.

The Saergan-nCIE, by its duration, magnitude and shape, requires a rapid onset and steady release of isotopically light carbon (likely CO_2; less likely CH_4) to overcompensate the effects of increased burial of C_{org}. In a second step, the initial effect should be successively counterbalanced (net-input of ^{13}C) *via* carbonate compensation (shifting lysoclines) and weathering feedbacks (Broecker & Peng, 1987; Weissert *et al*., 1998; Berner, 2003; Ridgwell & Zeebe, 2005; Tyrrell *et al*., 2007; Jenkyns, 2010; Vervoort *et al*., 2019). By now, there is independent evidence (notably Hg/TOC) for intense outgassing (CO_2, SO_2, H_2S) during the deposition of the lower part of the Saergan Formation (Liu *et al*., 2019b; Yao *et al*., 2021). The associated positive $\delta^{18}O$ anomaly (significant because $\geq |1.5|$) suggests short-term cooling. One possible scenario suggests climate change (cooling) whereby the total effect of outgassing of SO_2 and aerosols outcompetes the effect of CO_2 release (Lee & Dee, 2019). This view is coherent with the Middle Ordovician conversion of the Cathay-Tasman Province into an active continental arc (Cocks & Torsvik, 2020); cf. Zellmer *et al*. (2015); that is an active continental arc with inward-dipping double subduction (IDDS); Ge *et al*., (2014), Kiràly *et al*. (2021).

As an alternative, this anomaly might be due to the (implied) deepening of the depositional environment reaching into relatively cold and sub-/anoxic bottom waters. This scenario appears problematic because for the Saergan Formation, the nature of the microcrystalline carbonate present in its higher portion remains poorly understood (Zhang & Munnecke, 2016). Finally, there could be an issue in the form of a significant facies change in terms of granularity and the importance of diagenetic phases. The IDDS-related outgassing scenario (SO_2, aerosols) by impact (negative $\delta^{13}C$ anomaly, positive $\delta^{18}O$ anomaly, Hg/TOC) and time-scale is in accord with an ocean acidification episode implied from dwarfism and condensation (Fig. 5) and the subsequent demise of the Yijianfang sponge-pelmatozoan carbonate factory including the extinction of calathid (aragonitic) sponges (Fig. 19).

Short-term events (MDICE; GICE)

For the reasons mentioned above (context, age, shape, duration, magnitude), the signal of the MDICE is absent in the synoptic succession of the western Tarim Basin (Fig. 19). The chemostratigraphic datum labeled "MDICE?" by Zhang & Munnecke (2016; their Fig. 6) represents the intersection between the long-term rise in $\delta^{13}C$ values and the abrupt onset of the Saergan-nCIE (*Suecicus*-Event of Fig. 19). The chemostratigraphic datum labeled "SAICE" (Sandbian Positive Isotopic Carbon Excursion) by Zhang and Munnecke (2016) is problematic (Fig. 19). There is no short-term, significant (≥ 1) increase of $\delta^{13}C$ values. Indeed, SAICE is very poorly defined, appears restricted to Baltoscandia, and *hitherto* was never reported from graptolite-bearing strata (Bergstöm et al., 2020).

By contrast, in the western Tarim Basin there is convincing evidence for the GICE as defined by magnitude and age (Bergström et al., 2020), that is, a distinct $\Delta^{13}C_{carbonate} > +1$ located at or near the base of the *Diplacanthograptus caudatus* or *Belodina confluens* Zone, respectively (Fig. 19). Nevertheless (Fig. 19), the generalized GICE (as labelled by Zhang

& Munnecke, 2016) is highly skewed, starting with a rapid rise, reaching a distinct peak at +3.2 ‰ (tipping point of long-term trend) then tailing down smoothly, thereby resembling a baseline shift. The issue here is that GICE is a distinct short-term event and not the tipping point of a relatively smooth long-term trend. While in general accord with the chemostratigraphic labeling of Zhang & Munnecke (2016), with caution, it might be advantageous to constrain GICE to occur along the rapid rise of $\delta^{13}C$ values associated with a positive shift of $\delta^{18}O$ values (GICE of Fig. 19). This approach would preserve its event-character and its value for graphic correlation even if the GICE yet is not fully resolved and, at least for the insights gained here, appears to interfere with the establishment of a highly-productive carbonate factory with its associated geochemical impact due to photosynthesis and aragonite production (here the bahamite-type Lianglitag Formation).

Such a short-term (several 100s of thousand years) positive excursion of global extent conventionally is interpreted in terms of concurrent source rock formation (effective burial of C_{org}), enhanced primary production (photosynthesis) and the effects of silicate weathering associated with soil formation (Kump & Arthur, 1999; Payne & Kump, 2007). Here, extra options might apply because of the bahamite-type depositional context associated with the diversification of the marine flora. First, geochemically altered platform-top water masses might mix with open-marine water masses during transgressive events producing simultaneous positive shifts in $\delta^{13}C_{carbonate}$ and $\delta^{18}O_{carbonate}$ (Immenhauser *et al*., 2003). Second, there might be a significant shift of the carbonate mineralogy, in this case toward aragonite (Swart, 2008; Lécuyer *et al*., 2012).

At the scale of this study (Fig. 19), there is no obvious link to a GICE-concurrent black-shale deposit. However, an impact from increased burial of C_{org} should not be ruled out. This is because black-shales occur and re-occur in a diachronous fashion throughout the Katian of the Tarim Basin and its peripheral regions (Chen *et al*., 2012; Liu *et al*., 2016b). The mixing of geochemically distinct water masses appears unlikely because in its early stage, the Lianglitag Formation (L1) forms part of a high-energy carbonate ramp, lacking a seaward fringe of reefs, buildups or shoals, thus inhibiting the formation of spatially confined aqua-facies (discussion in Immenhauser *et al*., 2008). However, coincident with the GICE, there was a rapid biodiversification and a significant growing stock of calcareous algae (Riding & Fan, 2001; Shen & Neuweiler, 2016) performing photosynthesis and producing aragonite (cf. Verbruggen *et al*., 2009 for the phylogenesis and respective time estimates of early algae evolution).

In this view, the net effects of photosynthesis (cf. Geyman & Maloof, 2019) and aragonite production (Swart, 2008; Lécuyer *et al*., 2012) performed by the evolving calcareous green algae growing stock might have blurred GICE at regional scale. Taken together, the specific expression of the GICE in the western Tarim Basin (by context and shape, partial masquerade, baseline shift, indirect distinction *via* positive shift of $\delta^{18}O$ values) remains not fully resolved. The variation of shape and magnitude of the generalized GICE along a carbonate ramp-to-basin transect (cf. Zhang & Munnecke, 2016) should be reconsidered for systematic sampling and component-specific analysis expressed chronostratigraphically in 2-D (Swart, 2008).

CONCLUSIONS

(1) The Middle to Late Ordovician succession of the western Tarim Basin (China) displays a peculiar chronostratigraphic architecture and a distinct carbon-oxygen isotope record. This appears to be due to specific paleo(bio)geographic and paleotectonic conditions, being part of an agglomerate of terranes that switched from a passive to an active continental arc setting.

(2) The Darriwilian carbonate ramp system was dominated by filter feeders (pelmatozoa, sponges) and demised in concert with the global extinction of (aragonitic) calathid sponges. The environmental drowning unconformity is associated with condensation and pelmatozoan dwarfism followed by a multi-Myr lasting hiatus.

(3) Hiatus-correlative conformable deposits are black shales (Saergan Formation) preserved in slope to basin settings. These black shales hold a medium-term negative $\delta^{13}C$ excursion (Saergan-nCIE) associated with an initial positive $\delta^{18}O$ anomaly (*Suecicus*-Event). With caution and subject to further studies, a complex interplay of volcanism/outgassing, black shale formation and ocean acidification is implied. The *Suecicus*-Event together with the Saergan-nCIE masquerades the otherwise global middle Darriwilian positive $\delta^{13}C_{carbonate}$ excursion (MDICE).

(4) A Sandbian marine red-bed interval succeeds (Tumuxiuke Formation) indicating O_2-rich ferruginous bottom waters and re-establishing a long-term trend of increasing $\delta^{13}C$ values.

(5) This long-term trend culminates in the lowermost Katian Lianglitag Formation (at 3.2 ‰) followed by a steady decrease. The overall pattern appears to be global in extent, presumably expressing the relative rates of burial of disseminated C_{org} *versus* that of $C_{carbonate}$.

(6) Although yet not fully resolved, the lowermost Katian interval of rapidly rising $\delta^{13}C$ values associated with a positive shift of $\delta^{18}O$ values is interpreted to represent the globally reported Guttenberg carbon-isotope excursion (GICE). Its regional expression is interpreted to result from the combined effects of enhanced C_{org} burial and a boosting bahamite-type carbonate factory affecting the $\delta^{13}C$ record *via* photosynthesis and a significant (initial) amount of aragonite.

(7) This study asks for the application of multiple geochemical proxies to explore further the nature of the *Suecicus*-Event and to verify the significance of GICE along a carbonate ramp-to-basin transect.

ACKNOWLEDGEMENTS

YS acknowledges financial support from the Bourse Québec 2008, the China Scholarship Council Award and the CSPG PhD Thesis Award. Additional funding was obtained from the Faculty of Sciences and Engineering (Université Laval), Hefei University of Technology (No. JZ2018HGBZ0157; No. PA2018GDQT0007; No. PA2018GDQT0020), the Provincial Natural Science Foundation of Anhui (No. 1908085QD152), the National Natural Science Foundation of China (No. 41902104), the Hefei Innovation Program for Returned Overseas Students, the Key Laboratory of Stratigraphy and Palaeontology, China Ministry of Natural Resources (No. KLSP1903) and the Second Tibetan Plateau Scientific

Expedition and Research Program (2019QZKK0708). The authors are grateful to Dr. Dieter Buhl, Dr. Andrea Niedermayr and the staff of the geochemical laboratory at Ruhr-Universtät Bochum, Germany. We thank Dr. Rolf Neuser (Ruhr-Universtät Bochum, Germany) for assistance during cathodoluminescence microscopy. We acknowledge Prof. Bingsong Yu (China University of Geosciences, Beijing, China) for providing additional thin-section material. He together with Prof. Octavian Catuneanu (University of Alberta, Edmonton, Canada) also commented on the Wheeler diagram. Mr. Liu Changqing (Aksu) greatly assisted our field work. We thank Edmond Rousseau (Université Laval) for thin-section preparation. An earlier version of this paper benefitted from the comments of two anonymous journal reviewers. This paper is a contribution to the International Geoscience Programme Project (IGCP) 653 – The onset of the Great Ordovician Biodiversification Event and IGCP 735 – Rocks and the Rise of Ordovician Life.

CONFLICT OF INTEREST

There are no conflicts of interest.

DATA AVAILABILITY STATEMENT

Not applicable

REFERENCES

Ager, D.V. (1992) The nature of the stratigraphic record, 3rd edn. Wiley, Chichester, 151 pp.

Algeo, T.J., Marenco, P.J. and **Saltzman, M.R.** (2016) Co-evolution of oceans, climate, and the biosphere during the 'Ordovician Revolution': A review. *Palaeogeogr. Palaeoclimatol. Palaeoecol.*, **458**, 1–11.

Ausich, W.I. (1997) Regional encrinites: a vanished lithofacies. In: *Paleontological Events, Stratigraphic, Ecological and Evolutionary Implications* (Eds C.E. Brett and G.C. Baird), pp. 509–520. Columbia University Press, New York.

Baqués, V., Ukar, E., Laubach, S.E., Forstner, S.R. and **Fall, A.** (2020) Fracture, dissolution, and cementation events in Ordovician carbonate reservoirs, Tarim Basin, NW China. *Geofluids*, https://doi.org/10.1155/2020/9037429.

Bergström, S.M., Chen, X., Schmitz, B., Young, S., Rong, J. and **Saltzman, M.R.** (2009) First documentation of the Ordovician Guttenberg $\delta^{13}C$ excursion (GICE) in Asia: chemostratigraphy of the Pagoda and Yanwashan formations in southeastern China. *Geol. Mag.*, **146**, 1–11.

Bergström, S.M., Eriksson, M.E. and **Ahlberg, P.** (2020) Chapter Six - Ordovician $\delta^{13}C$ chemostratigraphy: A global review of major excursions and their ties to graptolite and conodont biostratigraphy. In: *Stratigraphy & Timescales volume 5: Carbon Isotope Stratigraphy* (Ed. M. Montenari), pp. 319–351, Academic Press, Cambridge.

Bergström, S.M., **Schmitz, B.**, **Saltzman, M.R.** and **Huff, W.D.** (2010a) The Upper Ordovician Guttenberg $\delta^{13}C$ excursion (GICE) in North America and Baltoscandia: Occurrence, chronostratigraphic significance, and paleoenvironmental relationships. In: *The Ordovician Earth System* (Eds S.C. Finney and W.B.N. Berry), *Geol. Soc. Am. Spec. Pap.*, 466, 37–67.

Bergström, S.M., **Young, S.** and **Schmitz, B.** (2010b) Katian (Upper Ordovician) $\delta^{13}C$ chemostratigraphy and sequence stratigraphy in the United States and Baltoscandia: a regional comparison. *Palaeogeogr. Palaeoclimatol. Palaeoecol.*, **296**, 217–234.

Berner, R. (2003) The long-term carbon cycle, fossil fuels and atmospheric composition. *Nature*, **426**, 323–326.

Berry, W.B.N. (2010) Black shales: An Ordovician perspective. In: *The Ordovician Earth System* (Eds S.C. Finney and W.B.N. Berry), *Geol. Soc. Am. Spec. Pap.*, 466, 141–147.

Bjørlykke, K. and **Jahren, J.** (2012) Open or closed geochemical systems during diagenesis in sedimentary basins: constraints on mass transfer during diagenesis and the prediction of porosity in sandstone and carbonate reservoirs. *AAPG Bull.*, **96**, 2193–2214.

Bodine, M.W., Jr and **Fernalld, T.H.** (1973) EDTA dissolution of gypsum, anhydrite, and Ca-Mg carbonates. *J. Sed. Petrol.*, **43**, 1152–1156.

Borths, M.R. and **Ausich, W.I.** (2011) Ordovician–Silurian Lilliput crinoids during the end-Ordovician biotic crisis. *Swiss Journal of Palaeontology*, **130**, 7–18.

Brand, U. and **Veizer, J.** (1981) Chemical diagenesis of a multicomponent carbonate system–2: Stable isotopes. *J. Sed. Petrol.*, **50**, 987–997.

Broecker, W.S. and **Peng, T.-H.** (1987) The role of calcium carbonate compensation in the glacial-interglacial atmospheric CO_2 change. *Global Biogeochem. Cycles*, **1**, 15–29.

Chang, X., **Hou, M.**, **Woods, A.**, **Chen, Z.-Q.**, **Liu, X.**, **Liao, Z.**, **Liu, Y.** and **Chao, H.** (2021) Late Ordovician paleoceanographic change: Sedimentary and geochemical evidence from Northwest Tarim and Middle Yangtze region, China. *Palaeogeogr. Palaeoclimatol. Palaeoecol.*, **562**, https://doi.org/10.1016/j.palaeo.2020.110070.

Chen, K., **Lv, X.**, **Qian, Y.**, **Wu, S.** and **Dong, S.** (2020) $\delta^{30}Si$ and $\delta^{18}O$ of multiple silica phases in chert: Implications for $\delta^{30}Si_{seawater}$ of Darriwilian seawater and sea surface temperatures. *Palaeogeogr. Palaeoclimatol. Palaeoecol.*, **544**, https://doi.org/10.1016/j.palaeo.2020.109584

Chen, X., **Zhang, Y.**, **Li, Y.**, **Fan, J.**, **Tang, P.**, **Chen, Q.** and **Zhang, Y.** (2012) Biostratigraphic correlation of the Ordovician black shales in Tarim Basin and its peripheral regions. *Science China Earth Sciences*, **55**, 1230–1237.

Christ, N., **Maerz, S.**, **Kutschera, E.**, **Kwiecien, O.** and **Mutti, M.** (2018) Palaeoenvironmental and diagenetic reconstruction of a closed-lacustrine carbonate system–the challenging marginal setting of the Miocene Ries Crater Lake (Germany). *Sedimentology*, **65**, 235–262.

Cocks, L.R.M. and **Torsvik, T.H.** (2020) Ordovician palaeogeography and climate change. *Gondwana Research*, **100**, 53–72.

Cui, H., Guan, P. and **Jian, X.** (2012) Magmatic hydrothermal fluids-formation water compound system and diagenetic response of carbonate reservoir rocks in northern Tarim Basin. *Acta Scientiarum Naturalium Universitatis Pekinensis*, **48**, 433–443 (in Chinese with English abstract).

Czerniakowski, L.A., **Lohmann, K.C.** and **Wilson, J.L.** (1984) Closed-system marine burial diagenesis: isotopic data from the Austin Chalk and its components. *Sedimentology*, **31**, 863–877.

Davies, G.R. and **Smith, L.B., Jr** (2006) Structurally controlled hydrothermal dolomite reservoir facies: An overview. *AAPG Bull.*, **90**, 1641–1690.

Dettman, D.L. and **Lohman, K.C.** (1995) Microsampling carbonates for stable isotope and minor element analysis: physical separation of samples on 20 micrometer scale. *J. Sed. Res.*, **65**, 566–569.

Dickson, J.A.D. (1965) A modified staining technique for carbonates in thin Section. *Nature*, **205**, 587.

Fantle, M.S., **Barnes, B.D.** and **Lau, K.V.** (2020) The role of diagenesis in shaping the geochemistry of the marine carbonate record. *Annu. Rev. Earth Planet. Sci.*, **48**, 549–583.

Fantle, M.S. and **Higgins, J.** (2014) The effects of diagenesis and dolomitization on Ca and Mg isotopes in marine platform carbonates: Implications for the geochemical cycles of Ca and Mg. *Geochim. Cosmochim. Acta*, **142**, 458–481.

Flügel, E. and **Flügel-Kahler, E.** (1992) Phanerozoic reef evolution: basic questions and data base. *Facie*s, **26**, 167–278.

Gao, Z. and **Fan, T.** (2013) Ordovician intra-platform shoal reservoirs in the Tarim Basin, NW China: Characteristics and depositional controls. *Bull. Can. Petrol. Geol.*, **61**, 83–100.

Ge, R., Zhu, W., Wilde, S.A., He, J., Cui, X., Wang, X. and **Zheng, B.** (2014) Neoproterozoic to Paleozoic long-lived accretionary orogeny in the northern Tarim Craton. *Tectonics*, **33**, 302–329.

Geyman, E.C. and **Maloof, A.C.** (2019) A diurnal carbon engine explains ^{13}C-enriched carbonates without increasing the global production of oxygen. *Proc. Natl Acad. Sci. USA.*, **116**, 24433–24439.

Hennige, S., **Roberts, J.M.** and **Williamson, P.** (2014) An Updated Synthesis of the Impacts of Ocean Acidification on Marine Biodiversity. Secretariat of the Convention on Biological Diversity, Technical Series No. 75, Montreal, 99 pp.

Hu, M., **Fu, X.**, **Cai, Q.**, **Yang, W.** and **Zhu, W.** (2014) Characteristics and genetic model of karst reservoirs of Ordovician Yingshan-Yijianfang Formation in Halahatang area, northern Tarim Basin. *Geology in China*, **41**, 1476–1486 (in Chinese with English abstract).

Huang, H., Zhang, S. and **Su, J.** (2016) Palaeozoic oil–source correlation in the Tarim Basin, NW China: A review. *Org. Geochem.*, **94**, 32–46.

Immenhauser, A. (2021) On the delimitation of the carbonate burial realm. *The Depositional Record*, https://doi.org/10.1002/dep2.173.

Immenhauser, A., Della Porta, G., Kenter, J.A.M. and **Bahamonde, J.R.** (2003) An alternative model for positive shifts in shallow-marine carbonate δ^{13}C and δ^{18}O. *Sedimentology*, **5**, 953–959.

Immenhauser, A., Holmden, C. and **Patterson, W.P.** (2008) Interpreting the carbon-isotope record of ancient shallow epeiric seas: lessons from the recent. In: *Dynamics of Epeiric Seas* (Eds B.R. Pratt and C. Holmden). *Geol. Assoc. Can. Spec. Pap.*, **48**, 135–174.

Jenkyns, H.C. (2010) Geochemistry of oceanic anoxic events. *Geochemistry, Geophysics, Geosystems*, **11**, https://doi.org/10.1029/2009GC002788.

Jiang, L., **Pan, W.**, **Cai, C.**, **Jia, L.**, **Pan, L.**, **Wang, T.**, **Li, H.**, **Chen, S.** and **Chen, Y.** (2014) Fluid mixing induced by hydrothermal activity in the Ordovician carbonates in Tarim Basin, China. *Geofluids*, **15**, 483–498.

Jiang, M., Zhu, J., Chen, D., Zhang, R. and **Qiao, G.** (2001) Carbon and strontium isotope variation and responses to sea-level fluctuations in the Ordovician of the Tarim Basin. *Science in China (Series D)*, **44**, 816–823.

Jiao, Y., Rong, H., Wang, R., Wu, L., Yan, J., Zeng, F., Gu, Y. and **Li, R.** (2011) Reservoir depositional system analysis of Ordovician carbonate platform margin in

Yijianfang ourcrops of western Tarim Basin. *Acta Petrologica Sinica*, **27**, 285–296 (in Chinese with English abstract).

Jiao, Y., Wu, L., Rong, H., Wang, Y. and **Wang, R.** (2012) Paleoecology of the Ordovician reef-shoal depositional system in the Yijianfang outcrop of the Bachu Area, West Tarim Basin. *Journal of Earth Science*, **23**, 408−420.

Király, Á., Funiciello, F., Capitanio, F.A. and **Faccenna, C.** (2021) Dynamic interactions between subduction zones. *Global Planet. Change*, **202**, https://doi.org/10.1016/j.gloplacha.2021.103501.

Kump, L.R. and **Arthur, M.A.** (1999) Interpreting carbon-isotope excursions: Carbonates and organic matter. *Chem. Geol.*, **161**, 181−198.

Land, L.S. (1995) Oxygen and carbon isotopic composition of Ordovician brachiopods: Implications for coeval seawater: Discussion. *Geochim. Cosmochim. Acta*, **59**, 2843−2844.

Lécuyer, C., Hutzler, A., Amiot, R., Daux, V., Grosheny, D., Otero, O., Martineau, F., Fourel, F., Balter, V. and **Reynard, B.** (2012) Carbon and oxygen isotope fractionations between aragonite and calcite of shells from modern molluscs. *Chem. Geol.*, **332−333**, 92−101.

Lee, C.-T. and **Dee, S.** (2019) Does volcanism cause warming or cooling. *Geology*, **47**, 687–688.

Li, Q., Li, Y., Zhang, Y. and **Munnecke, A.** (2017) Dissecting *Calathium*-microbial frameworks: The significance of calathids for the middle Ordovician reefs in the Tarim Basin, northwestern China. *Palaeogeogr. Palaeoclimatol. Palaeoecol.*, **474**, 66–78.

Li, S., Ren, J., Xing, F., Liu, Z., Li, H., Chen, Q. and **Li, Z.** (2012) Dynamic processes of the Paleozoic Tarim Basin and its significance for hydrocarbon accumulation – a review and discussion. *Journal of Earth Science*, **23**, 381–394.

Li, Y., Wang, J., Shen, A. and **Huang, Z.** (2007) Evolutionary significance of the *Calathium* reef mound from the Yijianfang Formation, Bachu, Xinjiang. *Acta Palaeontologica Sinica*, **46**, 347–354 (in Chinese with English abstract).

Li, Y., Huang, Z., Wang, J., Wang, Z., Xue, Y., Zhang, J., Zhang, Y., Fan, J. and **Zhang, Y.** (2009) Conodont biostratigraphy and sedimentology of the Middle and Upper Ordovician in Bachu, Xinjiang. *Journal of Stratigraphy*, **33**, 113–122 (in Chinese with English abstract).

Liao, T., Hou, J., Chen, L., Yang, W., Dong, Y. and **Bai, X.** (2016) Fault controlling on non-exposed karst fracture-vug reservoirs of the Ordovician in Halahatang oilfield, northern Tarim Basin. *Journal of Palaeogeography*, **18**, 221–235.

Liu, C., Li, G., Wang, D., Liu, Y., Luo, M. and **Shao, X.** (2016a) Middle–Upper Ordovician (Darriwilian–Early Katian) positive carbon isotope excursions in the northern Tarim Basin, Northwest China: Implications for stratigraphic correlation and paleoclimate. *Journal of Earth Science*, **27**, 317–328.

Liu, C., Li, G., Luo, M., Shao, X., Luo, P., Liu, Y. and **Gao, L.** (2016b) Stratigraphic correlation and source rock distribution of the Middle − Upper Ordovician in the Shaya Uplift and Kalpin outcrop, Tarim Basin. *Petroleum Geology & Experiment*, **38**, 170–177 (in Chinese with English abstract).

Liu, L., Liang, L., Wu, Y., Zhou, X., Jia, L. and **Riding, R.** (2020) Ordovician cyanobacterial calcification: A marine fossil proxy for atmospheric CO_2. *Earth Planet. Sci. Lett.*, **530**, https://doi.org/10.1016/j.epsl.2019.115950.

Liu, M., Chen, D., Zhou, X., Tang, D., Them II, T. R. and **Jiang, M.** (2019) Upper Ordovician marine red limestones, Tarim Basin, NW China: A product of an oxygenated deep ocean and changing climate? *Global Planet. Change*, **183**, https://doi.org/10.1016/j.gloplacha.2019.103032.

Liu, M., Chen, D., Zhou, X., Yuan, W., Jiang, M. and **Liu, L.** (2019) Climatic and oceanic changes during the Middle-Late Ordovician transition in the Tarim Basin, NW China and implications for the Great Ordovician Biodiversification Event. *Palaeogeogr. Palaeoclimatol. Palaeoecol.*, **514**, 522–535.

Ma, A., Jin, Z., Zhang, S. and **Wang, Y.** (2006) Molecular geochemical characteristics of Cambrian–Ordovician source rocks in Tarim Basin, NW China. *Geochimica*, **35**, 593–601 (in Chinese with English abstract).

Ma, L., Zhang, Z., Wang, G. and **Li, Y.** (2013) Microfacies of the carbonates and palaeogeography of the Saergan Formation (Middle–Upper Ordovician), Kalpin Stratigraphic Region, Tarim, NW China. *Acta Micropalaeontologica Sinica*, **30**, 344–352 (in Chinese with English abstract).

Machel, H.G. (2004) Concepts and models of dolomitization: A critical reappraisal. *Geol. Soc. London Spec. Publ.*, **235**, 7–63.

Menegatti, A.P., Weissert, H., Brown, R.S., Tyson, R.V., Farrimond, P., Strasser, A. and **Caron, M.** (1998) High-resolution $\delta^{13}C$ stratigraphy through the early Aptian “Livello Selli” of the Alpine Tethys. *Paleoceanography*, **13**, 530–545.

Moore, C.H. (2001) Carbonate Reservoirs: Porosity, Evolution and Diagenesis in a Sequence Stratigraphic Framework, Developments in Sedimentology 55. Elsevier Science, Amsterdam, 460 pp.

Morad, S., Ketzer, J.M. and **De Ros, L.F.** (2012) Linking diagenesis to sequence stratigraphy: integrated tool for deciphering and predicting reservoir quality distribution, In: *Linking diagenesis to sequence stratigraphy in sedimentary successions* (Eds S. Morad, J.M. Ketzer and L.F. De Ros), *Int. Assoc. Sedimentol. Spec. Publ.*, **45**, 1–36.

Müller, M., Igbokwe, O.A., Walter, B., Pederson, C.L., Riechelmann, S., Richter, D.K., Albert, R., Gerdes, A., Buhl, D., Neuser, R.D., Bertotti, G. and **Immenhauser, A.** (2020) Testing the preservation potential of early diagenetic dolomites as geochemical archives. *Sedimentology*, **67**, 849–881.

Munnecke, A., Zhang, Y., Liu, X. and **Cheng, J.** (2011) Stable carbon isotope stratigraphy in the Ordovician of South China. *Palaeogeogr. Palaeoclimatol. Palaeoecol.*, **307**, 17–43.

Neuser, R.D., Bruhn, F., Götze, J., Habermann, D. and **Richter, D.K.** (1995) Cathodoluminescence: methodology and application. *Zbl. Geol. Paläont. Teil I*, **H. 1/2**, 287–306.

Neuweiler, F., Larmagnat, S., **Molson, J.** and **Fortin-Morin, F.** (2014) Sponge spicules, silicification and sequence stratigraphy. *J. Sed. Res.*, **84**, 1107–1119.

Payne, J.L. and **Kump, L.R.** (2007) Evidence for recurrent Early Triassic massive volcanism from quantitative interpretation of carbon isotope fluctuations. *Earth Planet. Sci. Lett.*, **256**, 264–277.

Qing, H. and **Veizer, J.** (1994) Oxygen and carbon isotopic composition of Ordovician brachiopods: Implications for coeval seawater. *Geochim. Cosmochim. Acta*, **58**, 4429–4442.

Quinton, P.C. (2016) *The Ordovician climate: constraints from carbon and oxygen isotopes.* Ph.D. thesis, University of Missouri, Columbia, 164 pp.

Quinton, P.C., Law, S., Macleod, K.G., Herrmann, A.D., Haynes, J.T. and **Leslie, S.A.** (2018) Testing the early Late Ordovician cool-water hypothesis with oxygen isotopes from conodont apatite. *Geol. Mag.*, **155**, 1727–1741.

Rasmussen, C.M., Kröger, B., Nielsen, M.L. and **Colmenar, J.** (2019) Cascading trend of early Paleozoic marine radiations paused by late Ordovician extinctions. *Proc. Natl Acad. Sci. USA*, **116**, 7207–7213.

Ridgwell, A. and **Zeebe, R.E.** (2005) The role of the global carbonate cycle in the regulation and evolution of the Earth system. *Earth Planet. Sci. Lett.*, **234**, 299–315.

Richter, D.K., Götte, T., Götze, J. and **Neuser, R.D.** (2003) Progress in application of cathodoluminescence (CL) in sedimentary petrology. *Mineralogy and Petrology*, **79**, 127–466.

Riding, R. and **Fan, J.** (2001) Ordovician calcified algae and cyanobacteria, northern Tarim Basin subsurface, China. *Palaeontology*, **44**, 783–810.

Riechelmann, S., Mavromatis, V., Buhl, D., Dietzel, M. and **Immenhauser, A.** (2020) Controls on formation and alteration of early diagenetic dolomite: A multi-proxy $\delta^{44/40}$Ca, δ^{26}Mg, δ^{18}O and δ^{13}C approach. *Geochim. Cosmochim. Acta*, **283**, 167–183.

Rong, H., Jiao, Y., Wang, Y., Wu, L. and **Wang, R.** (2014) Distribution and geological significance of *Girvanella* within the Yijianfang Ordovician reef complexes in the Bachu area, West Tarim Basin, China. *Facies*, **60**, 685–702.

Saltzman, M.R. and **Thomas, E.** (2012) Chapter 11 Carbon isotope stratigraphy. In: *The Geologic Time Scale 2012* 1st edn (Eds F.M. Gradstein, J.G. Ogg, M. Schmitz and O. Ogg), pp. 221–246, Elsevier.

Schlanger, S.O. and **Douglas, R.G.** (1974) The pelagic ooze chalk-limestone transition and its implications for marine stratigraphy, In: *Pelagic Sediments: On Land and under the Sea* (Eds K.J. Hsü and H.C. Jenkyns), *Int. Assoc. Sedimentol. Spec. Publ.*, **1**, 117–14.

Schlager, W. (1999) Type 3 Sequence Boundaries, In: *Advances in Carbonate Sequence Stratigraphy: Application to Reservoirs, Outcrops and Models* (Eds P.M. Harris, A.H. Saller and T. Simo), SEPM Spec. Publ., **63**, 35–45.

Servais, T., Harper, D.A.T., Li, J., Munnecke, A., Owen, A.W. and **Sheehan, P.M.** (2009) Understanding the Great Ordovician Biodiversification Event (GOBE): Influences of paleogeography, paleoclimate, or paleoecology? *GSA Today*, **19**, 4–10.

Shen, Y. and **Neuweiler, F.** (2015) *Halysis* Høeg, 1932 in Ordovician carbonate mounds, Tarim Basin, NW China. *Palaios*, **30**, 692−706.

Shen, Y. and **Neuweiler, F.** (2016) Taphocoenoses and diversification patterns of calcimicrobes and calcareous algae, Ordovician, Tarim Basin, China. *Can. J. Earth Sci.*, **53**, 702−711.

Shen, Y. and **Neuweiler, F.** (2018) Questioning the microbial origin of automicrite in Ordovician calathid-demosponge carbonate mounds. *Sedimentoloty*, **65**, 303−333.

Shi, J. (2016) Microfacies characteristics and sedimentary environment of Ordovician carbonate rocks from Gucheng Region in Eastern Tarim Basin. *Northwestern Geology*, **49**, 61–68 (in Chinese with English abstract).

Shields, G.A., Carden, G.A., Veizer, J., Meidla, T., Rong, J. and **Li, R.** (2003) Sr, C, and O isotope geochemistry of Ordovician brachiopods: A major isotopic event around the Middle-Late Ordovician transition. *Geochim. Cosmochim. Acta*, **67**, 2005–2025.

Song, H., Jiang, G., Poulton, S.W., Wignall, P.B., Tong, J., Song, H., An, Z., Chu, D., Tian, L., She, Z. and **Wang, C.** (2017) The onset of widespread marine red beds and the evolution of ferruginous oceans. *Nature Communications*, **8**, https://doi.org/10.1038/s41467-017-00502-x.

Swart, P.K. (2008) Global synchronous changes in the carbon isotopic composition of carbonate sediments unrelated to changes in the global carbon cycle. *Proc. Natl Acad. Sci. USA*, **105**, 13741–13745.

Swart, P.K. (2015) The geochemistry of carbonate diagenesis: The past, present and future. *Sedimentology*, **62**, 1233–1304.

Turner, S.A., Cosgrove, J.W. and **Liu, J.** (2010) Controls on lateral structural variability along the Keping Shan Thrust Belt, SW Tien Shan Foreland, China, In: *Hydrocarbons in Contractional Belts* (Eds G.P. Goffey, J. Craig, T. Needham and R. Scott), *Geol. Soc. London Spec. Publ.*, 3**48**, 71−85.

Tyrrell, T., Schneider, B., Charalampopoulou, A. and **Riebesel, U.** (2007) Coccolithophores and calcite saturation state in the Baltic and Black Seas. *Biogeosciences Discussion*, **4**, 3581–3605.

Veizer, J. (1995) Oxygen and carbon isotopic composition of Ordovician brachiopods: Implications for coeval seawater: Reply. *Geochim. Cosmochim. Acta*, **59**, 2845−2846.

Veizer, J., Ala, D., Azmy, K., Bruckschen, P., Buhl, D., Bruhn, F., Carden, G.A.F., Diener, A., Ebneth, S., Godderis, Y., Jasper, T., Korte, C., Pawellek, F., Podlaha, O.G. and **Strauss, H.** (1999) $^{87}Sr/^{86}Sr$, $\delta^{13}C$ and $\delta^{18}O$ evolution of Phanerozoic seawater. *Chem. Geol.*, **161**, 59−88.

Verbruggen, H., Ashworth, M., LoDuca, S.T., Vlaeminck, C., Cocquyt, E., Sauvage, T., Zechman, F.W., Littler, D.S., Littler, M.M., Leliaert, F. and **De Clerck, O.** (2009) A multi-locus time-calibrated phylogeny of the siphonous green algae. *Molecular Phylogenetics and Evolution*, **50**, 642–653.

Vervoort, P., Adloff, M., Greene, S.E. and **Turner, S.K.** (2019) Negative carbon isotope excursions: an interpretive framework. *Environmental Research Letters*, **14**, https://doi.org/10.1088/1748-9326/ab3318.

Walker, L.J., Wilkinson, B.H. and **Ivany, L.C.** (2002) Continental drift and Phanerozoic carbonate accumulation in shallow-shelf and deep-marine settings. *The Journal of Geology*, **110**, 75–87.

Wang, J., Li, Y., Zhang, Y. and **Kershaw, S.** (2017a) A Middle Ordovician (Darriwilian) Calathium reef complex on the carbonate ramp of the northwestern Tarim Block, northwest China: A sedimentological approach. *Palaeogeogr. Palaeoclimatol. Palaeoecol.*, **474**, 58–65.

Wang, Q., Han, J., Li, H., Sun, Y., He, H. and **Ren, S.** (2019) Carbonate sequence architecture，sedimentary evolution and sea level fluctuation of the Middle and Lower Ordovician on outcrops at the northwestern margin of Tarim Basin. *Oil & Gas Geology*, **40**, 835–850 (in Chinese with English abstract).

Wang, R., Jiao, Y., Rong, H., Xing, F., Zeng, F., Li, R. and **Zhu, X.** (2012) Reef-shoal depositional model and reservoir qualities of middle Ordovician Yijianfang formation in Bachu, Tarim Basin. *Journal of China University of Petroleum*, **36**, 47–52, 59 (in Chinese with English abstract).

Wang, Z. and **Zhou, T.** (1998) Ordovician conodonts from western and northeastern Tarim and their significance. *Acta Palaeontologica Sinica*, **37**, 173−193.

Wang, Z., Zhang, Z., Wu, R., Zhen, Y., Zhang, Y. and **Li, H.** (2017b) Ordovician conodont biostratigraphy in the platform and slope facies of the Tarim Basin, Xinjiang: Evidence for a significant depositional gap and the absence of Dapingian Strata. *Journal of Stratigraphy*, **41**, 357−367 (in Chinese with English abstract).

Webby, B.D. (2004) Introduction, In: *The Great Ordovician Biodiversification Event* (Eds B.D. Webby, F. Paris, M.L. Droser and I.G. Percival), pp. 1−37, Columbia University Press, New York.

Webby, B.D., Paris, F., Droser, M.L. and **Percival, I.G.** (2004) The Great Ordovician Biodiversification Event. Columbia University Press, New York, 484 pp.

Weissert, H, Lini, A., Föllmi, K.B. and **Kuhn, O.** (1998) Correlation of Early Cretaceous carbon isotope stratigraphy and platform drowning events: a possible link? *Palaeogeogr. Palaeoclimatol. Palaeoecol.*, **137**, 189−203.

Xiong, J., Wu, T. and **Ye, D.** (2006) New advances on the study of Middle–Late Ordovician conodonts in Bachu, Xinjiang. *Acta Palaeontologica Sinica*, **45**, 359−373 (in Chinese with English abstract).

Yao, H., Chen, X., Yin, R., Grasby, S.E., Weissert, H., Gu, X. and **Wang, C.** (2021) Mercury Evidence of Intense Volcanism Preceded Oceanic Anoxic Event 1d. *Geophys. Res. Lett.*, **49**, https://doi.org/10.1029/2020GL091508.

Zellmer, G., Edmonds, M. and **Straub, S.** (2015) The role of volatiles in the genesis, evolution and eruption of arc magmas, *Geol. Soc. London Spec. Publ.*, **410**, 292pp.

Zhang, S.C., Liang, D.G., Li, M.W., Xiao, Z.Y. and **He, Z.H.** (2002) Molecular fossils and oil–source rock correlations in Tarim Basin, NW China. *Chinese Science Bulletin*, **47**, 20–27 (in Chinese with English abstract).

Zhang, Y., Li, Y. and **Munnecke, A.** (2014a) Late Ordovician microbial reefs in the Lianglitag Formation (Bachu, Tarim, NW China). *Facies*, **60**, 663–684.

Zhang, Y., Lv, X., Yang, H., Han, J., Lan, X., Zhao, Y. and **Zhang, J.** (2014b) Control of hydrocarbon accumulation by Lower Paleozoic cap rocks in the Tazhong Low Rise, Central Uplift, Tarim Basin, West China. *Petroleum Science*, **11**, 67–80.

Zhang, Y., Wang, J., Munnecke, A. and **Li, Y.** (2015) Ramp morphology controlling the facies differentiation of a Late Ordovician reef complex at Bachu, Tarim Block, NW China. *Lethaia*, **48**, 509–521.

Zhang, Y. and **Munnecke, A.** (2016) Ordovician stable carbon isotope stratigraphy in the Tarim Basin, NW China. *Palaeogeogr. Palaeoclimatol. Palaeoecol.*, **458**, 154–175.

Zhao, Z., Zhang, G. and **Xiao, J.** (2000) Paleozoic Stratigraphy and Conodonts in Xinjiang. Petroleum Industry Press, Beijing, 340 pp (in Chinese).

Zhao, Z., Pan, W., Zhang, L., Deng, S. and **Huang, Z.** (2009) Sequence stratigraphy in the Ordovician in the Tarim Basin. *Geotectonica et Metallogenia*, **33**, 175–188 (in Chinese with English abstract).

Zhao, Z., Chen, X., Pan, M., Wu, X., Zheng, X. and **Pan, W.** (2010) Milankovitch Cycles in the Upper Ordovician Lianglitage Formation in the Tazhong—Bachu Area, Tarim Basin. *Acta Geol. Sinica*, **84**, 518–536 (in Chinese with English abstract).

Zhao, Z., Wu, M. and **Lai, J.** (2018) Unconformity between Lower Ordovician and Overlying Strata in Tarim Basin. *Xinjiang Petroleum Geology*, **39**, 530–536 (in Chinese with English abstract).

Zhou, Z., Chen, X., Wang, Z., Wang, Z., Li, J., Gen, L., Fang, Z., Qiao, X. and **Zhang, T.** (1990) Ordovician, In: *Biostratigraphy and geological evolution of Tarim* (Eds Z. Zhou and P. Chen), pp. 56−130, Science Press, Beijing (in Chinese).

Zhu, G., Zhang, S., Su, J., Zhang, B., Yang, H., Zhu, Y. and **Gu, L.** (2013) Alteration and multi-stage accumulation of oil and gas in the Ordovician of the Tabei Uplift, Tarim Basin, NW China: Implications for genetic origin of the diverse hydrocarbons. *Mar. Petrol. Geol.*, **46**, 234–250.

Supplementary Data File: Carbon and Oxygen Stable Isotope Values present in the Middle to Late Ordovician succession at Bachu Uplift, western Tarim Basin, Bachu (Maralbexi) county, Xinjiang Uyghur Autonomous Region, NW China

lab number	sample name	mineral	Specific component	sample weight [mg]	max. amplitude [V]	corrected values			
						d$^{13}C_{PDB}$ [‰]	± s	d$^{18}O_{PDB}$ [‰]	± s
YF 1	1-2-5	calcite	C4	0.40	6443	0.55	0.04	-5.31	0.03
YF 2	1-2-5	calcite	AM1	0.41	6129	0.65	0.04	-5.75	0.03
YF 3	1-2-5	calcite	AM3	0.41	6240	0.68	0.04	-6.57	0.05
YF 4	1-2-5	calcite	AM1	0.45	7496	0.78	0.03	-6.11	0.03
YF 5	1-2-5	calcite	AM1	0.41	6265	0.84	0.03	-6.22	0.04
YF 6	1-2-5	calcite	AM5	0.47	7500	0.77	0.04	-6.06	0.04
YF 7	1-2-5	calcite	AM4	0.41	5989	0.28	0.04	-7.23	0.03
YF 8	1-2-5	calcite	Bry	0.39	5742	0.19	0.04	-7.72	0.06
YF 9	1-2-5	calcite	C1-C3	0.39	5935	0.53	0.03	-5.42	0.03
YF 10	1-1-5-2	calcite	AM1	0.43	6485	0.58	0.02	-5.33	0.04
YF 10	1-1-5-2	calcite	AM1	0.45	7120	0.62	0.02	-5.23	0.05
YF 11	1-1-5-2	calcite	C4	0.44	7034	0.41	0.03	-5.19	0.03
YF 12	1-1-5-2	calcite	C1-C2	0.43	6422	0.64	0.03	-5.84	0.04
YF 13	1-1-5-2	calcite	C1-C2	0.48	7188	0.76	0.03	-5.51	0.04
YF 15	1-1-5-2	calcite	C4	0.48	7600	1.01	0.04	-6.70	0.04
YF 16	1-1-7	calcite	Echinoderm	0.44	7156	0.60	0.02	-5.38	0.03
YF 17	1-1-7	calcite	Rfc+Ra	0.42	6890	0.63	0.03	-6.62	0.03
YF 18	1-1-7	calcite	Bra	0.41	5331	0.66	0.02	-5.63	0.04
YF 19	1-1-7	calcite	Bry	0.43	7435	0.62	0.05	-5.63	0.05
YF 19	1-1-7	calcite	Bry	0.45	7635	0.59	0.03	-5.60	0.06
YF 20	1-1-7	calcite	AM1	0.42	5956	0.61	0.04	-5.40	0.04
YF 21	1-1-7	Silica (40%) + ferroan calcite	Rfc+Ra	0.72	9207	0.66	0.03	-5.24	0.04
YF 22	1-2-3	calcite	C8	0.41	5937	0.03	0.05	-8.46	0.06
YF 23	1-2-3	calcite	C8	0.45	6957	0.24	0.03	-8.75	0.03
YF 24	22-1-4	calcite	C1-C2	0.40	6510	0.77	0.04	-5.64	0.05

YF 25	22-1-4	calcite	C1-C3	0.43	6791	0.72	0.05	-5.30	0.06
YF 26	3-1-3-2	calcite	M1	0.41	6045	2.56	0.03	-6.62	0.04
YF 27	3-1-3-2	calcite	M2	0.42	7075	2.37	0.03	-7.40	0.06
YF 28	3-1-3-2	calcite	M6	0.41	5594	2.43	0.03	-8.61	0.04
YF 28	3-1-3-2	calcite	M6	0.45	7390	2.44	0.03	-8.58	0.03
YF 29	3-1-3-2	calcite	C1-C2	0.44	7556	2.42	0.03	-7.08	0.05
YF 30	3-1-3-2	calcite	C3	0.46	7393	2.33	0.02	-8.71	0.05
YF 31	3-1-3-2	calcite	C5	0.42	6883	2.45	0.04	-9.72	0.03
YF 32	3-1-3-2	calcite	Rfc	0.43	7126	2.24	0.03	-9.70	0.05
YF 33	3-1-3-2	calcite	C8	0.47	7449	2.37	0.04	-9.28	0.06
YF 34	3-1-7	calcite	M4	0.43	6187	2.42	0.03	-6.91	0.05
YF 35	3-1-7	calcite	C5	0.43	7607	2.53	0.02	-9.01	0.04
YF 36	3-1-7	calcite	C6	0.46	7453	2.55	0.02	-6.72	0.02
YF 37	3-1-7	calcite	C6	0.43	7356	2.44	0.03	-6.59	0.03
YF 37	3-1-7	calcite	C6	0.42	6149	2.40	0.03	-6.66	0.03
YF 38	3-1-7	calcite	C10	0.42	6349	2.48	0.04	-10.70	0.03
YF 39	11-1-1	calcite	C10	0.43	6733	2.50	0.03	-10.78	0.04
YF 40	12-1-5	calcite	C2-C3	0.47	7683	2.71	0.03	-6.24	0.04
YF 41	12-1-5	calcite	M3	0.41	6585	2.53	0.03	-6.50	0.04
YF 42	12-1-5	calcite	M3	0.41	6017	2.59	0.03	-6.49	0.06
YF 43	12-1-5	calcite	C7	0.40	6454	2.73	0.02	-7.81	0.05
YF 43	12-1-5	calcite	C7	0.44	7194	2.75	0.02	-7.81	0.03
YF 44	12-1-5	calcite	C1-C2	0.40	6448	2.80	0.04	-5.83	0.04
YF 45	12-1-5	calcite	C1-C2	0.45	6821	2.95	0.01	-4.97	0.04
YF 46	12-1-5	calcite	Rfc	0.44	6556	2.35	0.03	-8.55	0.04
YF 47	12-1-5	calcite	C5	0.43	6494	2.77	0.03	-9.37	0.04
YF 48	12-1-5	calcite	M2	0.46	7096	2.80	0.04	-6.27	0.04
YF 49	11-1-1	calcite	C8	0.44	7138	2.29	0.02	-9.05	0.04
YF 50	18-1-3	calcite	C4	0.43	7166	2.59	0.04	-7.95	0.02
YF 50	18-1-3	calcite	C4	0.43	7248	2.55	0.02	-7.94	0.05
YF 51	18-1-3	dolomite	D3	0.43	6627	2.72	0.05	-9.36	0.03
YF 52	18-1-3	calcite	Echinoderm	0.46	7882	2.33	0.04	-4.03	0.06
YF 53	17-1-5	calcite	C1	0.46	7645	2.87	0.05	-7.02	0.04

YF 54	17-1-5	calcite	C3	0.44	7243	2.84	0.05	-7.07	0.04
YF 55	5-1-1	calcite	C1	0.44	7022	2.84	0.03	-4.82	0.04
YF 56	5-1-1	calcite	C1	0.42	7122	2.87	0.03	-5.20	0.03
YF 57	5-1-1	calcite	C1	0.39	6488	2.82	0.04	-5.08	0.04
YF 58	5-1-1	calcite	C1	0.47	7225	2.72	0.04	-4.69	0.05
YF 59	5-1-1	calcite	C5	0.42	6757	2.50	0.04	-9.17	0.03
YF 60	5-1-1	calcite	C2-C3	0.45	7381	2.58	0.03	-6.12	0.03
YF 61	5-1-1	calcite	Bryozoan	0.40	6729	2.47	0.03	-5.90	0.02
YF 62	5-1-1	calcite	M1	0.40	5894	2.58	0.03	-6.12	0.04
YF 63	5-1-1	calcite	C1-C2	0.41	6909	2.84	0.03	-4.97	0.04
YF 63	5-1-1	calcite	C1-C2	0.43	7658	2.81	0.04	-4.85	0.05
YF 64	5-1-1	calcite	C1-C2	0.45	7511	2.71	0.02	-5.15	0.05
YF 65	5-1-1	dolomite	D2	0.40	6352	2.14	0.03	-11.21	0.04
YF 66	5-1-1	dolomite	D3	0.41	6755	2.67	0.04	-9.03	0.04
YF 67	5-1-1	calcite	Algal pellets	0.41	7053	2.61	0.04	-6.25	0.06
YF 68	20-1-5	calcite	Luminescent brachiopod shell	0.41	6980	2.57	0.03	-5.94	0.04
YF 69	20-1-5	calcite	Luminescent brachiopod shell	0.45	7141	2.65	0.02	-5.60	0.04
YF 70	20-1-5	calcite	C1-C2	0.44	7200	2.63	0.03	-5.55	0.04
YF 71	20-1-5	calcite	C1-C3	0.42	6785	2.65	0.04	-5.60	0.05
YF 71	20-1-5	calcite	C1-C3	0.43	6958	2.67	0.01	-5.65	0.03
YF 72	20-1-5	calcite	Rfc	0.42	6824	2.60	0.03	-9.33	0.02
YF 73	20-1-5	calcite	Algal pellets	0.40	5935	2.58564	0.03	-6.1688	0.04
YF 74	20-1-5	calcite	*Apidium*	0.36	5420	2.74282	0.03	-5.4319	0.04
YF 75	20-1-5	calcite	C1	0.43	6971	2.78672	0.03	-5.2656	0.03
YF 76	18-1-3	calcite	Non-luminescent trilobite hash	0.42	6953	2.77943	0.03	-3.3639	0.04
YF 77	13-1-4	calcite	C1	0.42	6808	2.05	0.04	-7.09	0.05
YF 78	13-1-4	calcite	C1	0.46	7586	2.02	0.03	-7.51	0.03
YF 78	13-1-4	calcite	C1	0.45	7192	2.03	0.03	-7.39	0.03
YF 79	13-1-4	calcite	C1	0.40	6324	2.01	0.04	-7.21	0.06
YF 80	20-1-1	calcite	Non-luminescent brachiopod shell	0.40	6079	2.85	0.04	-2.99	0.05
YF 81	21-1-1	dolomite	D2	0.40	5767	2.38	0.02	-10.15	0.03
YF 82	21-1-1	calcite	C1	0.45	7287	3.15	0.02	-4.73	0.03
YF 83	18-1-7	calcite	*Apidium*	0.39	6077	2.78	0.04	-5.51	0.05

YF 84	18-1-7	calcite	C1-C2	0.42	6620	2.60	0.03	-6.33	0.04
YF 85	18-1-7	calcite	C8	0.41	6657	2.58	0.02	-9.14	0.04
YF 85	18-1-7	calcite	C8	0.42	6783	2.58	0.02	-9.10	0.04
YF 86	18-1-7	dolomite	D2	0.40	6093	2.51	0.04	-10.44	0.04
YF 87	18-1-7	calcite	C1-C2	0.46	7659	2.85	0.02	-5.62	0.04
YF 88	18-1-7	calcite	M2	0.40	6350	2.67	0.03	-5.43	0.04
YF 89	18-1-7	calcite	C2-C3	0.46	7951	2.67	0.03	-5.76	0.05
YF 90	18-1-7	calcite	C2-C3	0.39	6473	2.67	0.04	-5.78	0.04
YF 91	18-1-7	calcite	C2-C3	0.40	6596	2.72	0.02	-5.61	0.04
YF 91	18-1-7	calcite	C2-C3	0.40	6613	2.68	0.03	-5.65	0.04
YF 92	18-1-4	calcite	C2-C3	0.41	6437	2.77	0.03	-5.37	0.06
YF 93	18-1-4	calcite	C1-C2	0.39	5946	2.85	0.03	-4.65	0.04
YF 94	18-1-4	calcite	C1-C2	0.42	6600	2.74	0.03	-5.21	0.03
YF 95	20-1-3	calcite	Echinoderm	0.42	6651	2.53	0.04	-6.93	0.05
YF 96	20-1-3	calcite	Non-luminescent brachiopod shell	0.47	7567	2.91	0.02	-4.62	0.04
YF 97	4-1-3	calcite	C1	0.45	7597	2.59	0.03	-6.41	0.06
YF 98	12-2-4	calcite	*Girvanella*	0.40	5790	2.23	0.06	-4.90	0.04
YF 99	12-2-4	calcite	M4	0.42	7132	2.27	0.03	-5.27	0.04
YF 100	12-2-4	calcite	D4	0.49	8487	1.82	0.03	-7.24	0.04
YF 101	12-2-4	calcite	M5	0.41	6586	2.27	0.05	-7.30	0.05
YF 101	12-2-4	calcite	M5	0.43	7059	2.28	0.03	-7.35	0.04
YF 102	12-2-4	calcite	M3	0.42	6796	2.21	0.04	-6.23	0.06
YF 103	4-1-3	calcite	C1	0.40	6837	2.48	0.03	-7.18	0.05
YF 104	12-2-3	calcite	C10	0.46	7913	2.14	0.02	-10.72	0.03
YF 105	12-2-3	calcite	C10	0.45	6934	2.28	0.05	-10.05	0.03
YF 106	12-2-3	calcite	C1	0.41	6514	2.51	0.04	-6.08	0.04
YF 107	18-1-7	calcite	C1-C2	0.44	6633	3.08	0.05	-4.51	0.02
YF 108	18-1-7	calcite	C1-C2	0.47	7174	2.93	0.04	-5.36	0.04
YF 109	18-1-7	dolomite	D2	0.45	6813	2.54	0.03	-10.10	0.05
YF 110	19-1-1	calcite	Micrite	0.44	5920	1.32	0.02	-4.93	0.07
YF 111	20-1-1	calcite	Non-luminescent brachiopod shell	0.42	6387	2.39	0.05	-3.99	0.05
YF 112	20-1-1	calcite	C1-C2	0.46	6917	2.52	0.05	-4.22	0.07
YF 113	20-1-1	calcite	C1-C2	0.47	7371	2.41	0.03	-4.51	0.03

YF 114	5-1-1	calcite	C1	0.45	6985	2.89	0.03	-5.27	0.03
YF 114	5-1-1	calcite	C1	0.45	7110	2.84	0.03	-5.26	0.04
YF 115	2-1-1	dolomite	D-2	0.43	5732	-0.37	0.03	-11.25	0.04
YF 116	2-1-1	Ankerite+FeC; Silica 30%	Rfc+Ra	0.64	9978	-0.30	0.01	-6.21	0.02
YF 117	2-1-1	Ankerite+FeC; Silica 40%	Rfc+Ra	0.76	13057	0.38	0.03	-5.91	0.05
YF 118	3-1-5	Ankerite+FeC; Silica 50%	Rfc+Ra	0.86	14968	2.38	0.04	-7.83	0.05
YF 119	3-1-5	calcite	C6	0.41	6356	2.38	0.02	-6.66	0.03
YF 120	1-1-7	calcite	C4	0.41	6195	0.52	0.02	-5.61	0.04
YF 121	2-1-2	calcite	Rfc+Ra	0.45	6599	0.68	0.05	-6.03	0.05
YF 121	2-1-2	calcite	Rfc+Ra	0.42	5996	0.68	0.04	-5.98	0.06
YF 122	1-1-7	calcite	C1-C2	0.40	6459	0.78	0.03	-5.35	0.06
YF 123	22-1-4	calcite	C2-C3	0.45	6974	0.89	0.03	-5.36	0.04
YF 124	22-1-4	calcite	C3-C4	0.42	6562	0.33	0.05	-5.05	0.05
YF 125	1-1-5-1	calcite	C2-C3	0.48	5341	0.66	0.03	-5.13	0.05
YF 126	2-1-2	dolomite	D-2	0.43	5852	-0.32	0.04	-9.64	0.03
YF 127	20-1-1	calcite	Non-luminescent brachiopod shell	0.24	3816	2.57	0.05	-4.12	0.06
YF 128	1-1-5-1	calcite	IS3-IS4	0.37	6130	0.61	0.04	-5.52	0.04
YF 129	1-1-5-1	calcite	IS3-IS4	0.44	6569	0.90	0.04	-5.64	0.04
YF 130	1-1-7	calcite	AM5	0.40	5493	0.65	0.03	-5.64	0.07
YF 130	1-1-7	calcite	IS1	0.45	6786	0.64	0.02	-5.57	0.05
YF 131	1-1-5-1	calcite	IS1	0.42	5962	0.62	0.04	-5.46	0.04
YF 132	1-1-8	calcite		0.40	6235	0.70	0.03	-5.71	0.03
YF 133	1-1-8	calcite	AM4	0.42	6342	0.57	0.03	-5.36	0.05
YF 134	1-1-5-1	calcite	C7	0.33	5016	0.39	0.04	-7.09	0.04
YF 135	1-1-8	calcite	AM2	0.39	5908	0.83	0.04	-5.63	0.05
YF 136	1-1-5-1	calcite	AM1	0.41	6196	0.84	0.03	-5.66	0.04
YF 137	1-1-7	calcite	AM1	0.44	6346	0.64	0.03	-6.33	0.04
YF 138	5-1-1	calcite	C1	0.41	6332	2.87	0.03	-4.98	0.03
YF 139	1-2-1	calcite	C5	0.44	6946	0.18	0.04	-10.33	0.05
YF 140	1-1-4	calcite	C1-C2	0.39	5403	0.72	0.02	-5.64	0.05
YF 140	1-1-4	calcite	C1-C2	0.39	5517	0.73	0.03	-5.56	0.05
YF 141	1-1-4	Ankerite+FeC; Silica 40%	Rfc+Ra	0.84	11810	0.85	0.03	-5.74	0.05
YF 142	5-1-1	calcite	C3	0.47	6984	2.57	0.04	-7.55	0.02

YF 143	5-1-1	calcite	C5	0.43	6502	2.71	0.03	-9.54	0.03
YF 144	12-1-4	calcite	Bulk rock	0.46	7062	2.46	0.03	-5.75	0.03
YF 145	1-1-4	calcite	C3-C4	0.40	6049	0.75	0.04	-6.19	0.04
YF 146	5-1-1	calcite	C1-C3	0.44	6956	2.75	0.04	-5.68	0.03
YF 147	1-1-7	calcite	Bulk rock	0.41	6372	0.62	0.03	-5.77	0.07
YF 148	2-1-3	calcite	Bulk rock	0.45	6500	-0.24	0.03	-5.95	0.06
YF 149	3-1-3-2	calcite	Bulk rock	0.45	6969	2.41	0.03	-8.11	0.05
YF 149	3-1-3-2	calcite	Bulk rock	0.41	5703	2.40	0.04	-7.98	0.05